UNIVERSITÀ DI PISA

Scuola di Dottorato in Ingegneria “Leonardo da Vinci”

Corso di Dottorato di Ricerca in Ingegneria dell’Informazione: Elettronica, Informatica, Telecomunicazioni

Tesi di Dottorato di Ricerca

Computational intelligence techniques for maritime and coastal remote sensing

Autore:

Linda Corucci ______________________

Relatori:

Prof. Beatrice Lazzerini ______________________

Prof. Francesco Marcelloni ______________________

Ing. Andrea Masini ______________________

Ing. Marco Cococcioni ______________________

Anno 2011
SSD ING-INF/05

Abstract

The aim of this thesis is to investigate the potential of computational intelligence techniques for some applications in the analysis of remotely sensed multi-spectral images. In particular, two problems are addressed. The first one is the classification of oil spills at sea, while the second one is the estimation of sea bottom depth. In both cases, the exploitation of optical satellite data allows to develop operational tools for easily accessing and monitoring large marine areas, in an efficient and cost effective way.

Regarding the oil spill problem, today public opinion is certainly aware of the huge impact that oil tanker accidents and oil rig leaks have on marine and coastal environment. However, it is less known that most of the oil released in our seas cannot be ascribed to accidental spills, but rather to illegal ballast waters discharge, and to pollutant dumping at sea, during routine operations of oil tankers. For this reason, any effort for improving oil spill detection systems is of great importance. So far, Synthetic Aperture Radar (SAR) data have been preferred to multi-spectral data for oil spill detection applications, because of their all-weather and all-day capabilities, while optical images necessitate of clear sky conditions and day-light. On the other hand, many features make an optical approach desirable, such as lower cost and higher revisit time. Moreover, unlike SAR data, optical data are not affected by sea state, and are able to reduce false alarm rate, since they do not suffer from the main false alarm source in SAR data, that is represented by the presence of calm sea regions. In this thesis the problem of oil spill classification is tackled by applying different machine learning techniques to a significant dataset of regions of interest, collected in multi-spectral satellite images, acquired by MODIS sensor. These regions are then classified in one of two possible classes, that are *oil spills* and *look-alikes*, where *look-alikes* include any phenomena other than oil spills (e.g. algal blooms...). Results show that efficient and reliable oil spill classification systems based on optical data are feasible, and could offer a valuable support to the existing satellite-based monitoring systems.

The estimation of sea bottom depth from high resolution multi-spectral satellite images is the second major topic of this thesis. The motivations for dealing with this problem arise from the necessity of limiting expensive and time consuming measurement campaigns. Since satellite data allow to quickly analyse large areas, a solution for this issue is to employ intelligent techniques, which, by exploiting a small set of depth measurements, are able to extend bathymetry estimate to a much larger area, covered by a multi-spectral satellite image. Such techniques, once that the training phase has been completed, allow to achieve very accurate results, and, thanks to their generalization capabilities, provide reliable bathymetric maps which cover wide areas. A crucial element is represented by the training dataset, which is built by coupling a number of depth measurements, located in a limited part of the image, with corresponding radiances, acquired by the satellite sensor. A successful estimate essentially depends on how the training dataset resembles the rest of the scene. On the other hand, the result is not affected by model uncertainties and systematic errors, as results from model-based analytic approaches are. In this thesis a neuro-fuzzy technique is applied to two case studies, more precisely, two high resolution multi-spectral images related to the same area, but acquired in different years and in different meteorological conditions. Different situations of in-situ depths availability are considered in the study, and the effect of limited in-situ data availability on performance is evaluated. The effect of both meteorological conditions and training set size reduction on the overall performance is also taken into account. Results outperform previous studies on bathymetry estimation techniques, and allow to give indications on the optimal paths which can be adopted when planning data collection at sea.

Preface

This thesis is organized as follows: Chapter One gives an overview of satellite sensors for remote sensing of the marine environment. In particular, attention is focused on optical sensors, and on how these sensors are able to collect information regarding some properties of sea water and of its constituents. An introduction to some radiometric quantities useful to understand radiative transfer in atmosphere and in water is also given (Section 1.3.1). Then, a brief description of the apparent and inherent water optical properties follows (Section 1.3.2 and Section 1.3.3). Thus, this first chapter aims at introducing the reader to the context where this work is placed, that is the remote sensing of marine environment based on optical satellite data.

Chapter Two describes most of the methods which have been presented in the literature for retrieving information on water optical properties from remotely sensed optical images. Most contributions are about retrieving sea water constituent properties and bottom depth estimation. Two branches of techniques are described in this chapter, that are model-based analytical techniques (Section 2.1) and computational intelligence-based techniques (Section 2.2). The latter are usually employed in combination with model-based techniques, or use simulated training dataset based on theoretical models.

Chapter Three describes the approach to the use of computational intelligence techniques adopted in this thesis for remote sensing applications. It is a purely experimental approach, that abandons any model assumption, and is based solely on data. All techniques described in Chapter Three are used for the two applications presented in the following chapters.

Chapter Four reports the application to oil spill classification. First an introduction to the problem of oil pollution at sea is given. Then, some physical and chemical properties of different types of hydrocarbon compounds are briefly outlined, followed by the optical properties (Section 4.2.1 and Section 4.2.2). Attention is focused on the creation of a contrast between oil and water, which is responsible for the possibility of detecting oil spills by means of optical sensors (Section 4.2.3). This helps to understand the mechanisms that allow to detect oil spills from remote sensors, which are described in Section 4.3. Since, up to now, the problem of oil spills has been tackled mainly by exploiting SAR sensors, in Section 4.3.1 a review of oil spill detection and classification techniques, developed for SAR data, is given. Section 4.4 describes the advantages and using optical data, and reports some previous works presented in the literature. The following sections describe the proposed approach (Section 4.5), the dataset (Section 4.6), the features used to characterize oil spills (Section 4.7), and different classification systems that have been employed, starting with a simple batch approach (Section 4.8), improving the batch approach (Section 4.9) and concluding with an online cost-oriented approach (Section 4.10), showing the achieved results.

Chapter Five reports the application to bathymetry estimation from high resolution multi-spectral satellite images. In particular, a review of different approaches to bathymetry estimation from satellite data is given in Section 5.2, then, in Section 5.3, two case studies are presented. Section 5.4.1 describes the results obtained in the first case study, that is characterized by optimal sea conditions, and a significant dataset of in-situ depth measurements. Different situations of limited in-situ data availability are also analysed. Section 5.4.2 reports the results obtained in the second case study, characterized by unfavourable sea conditions and limited in-situ data availability.

Finally, Section 6 draws some conclusions.

Table of Contents

List of Figures

List of Tables

List of Symbols, Abbreviations and Nomenclature

Symbol	Definition
ANFIS	Adaptive Network-based Fuzzy Inference System
AOPs	Apparent Optical Properties
API	American Petroleum Institute
AUC	Area Under ROC Curve
CDOM	Coloured Dissolved Organic Matter
EO	Earth Observation
FPR	False Positive Rate
GA	Genetic Algorithm
IFOV	Instantaneous Field Of View
IOPs	Inherent Optical Properties
IR	Infrared
LSE	Least Square Estimate
MLP	Multi Layer Perceptron
MODIS	Moderate Resolution Imaging Spectroradiometer
MW	Microwave
NIR	Near Infrared
PCA	Principal Component Analysis
RBF	Radial Basis Function
REA	Rapid Environmental Access
ROC	Receiver Operating Characteristic
SAR	Synthetic Aperture Radar
SG	Specific Gravity
SLAR	Side-Looking Airborne Radar
SVM	Support Vector Machine
TOA	Top Of Atmosphere
TPR	True Positive Rate
UV	Ultraviolet
VIS	Visible

Chapter One: Remote sensing of the marine environment: basic concepts

1.1 Overview

Today, a wide variety of sensors, mounted on satellite platforms, is employed for Earth Observation (EO) activities, devoted to environmental monitoring. These sensors continuously acquire images of our planet, providing an extensive coverage across both space and time, and allowing the scientific remote sensing community to analyse a number of phenomena which may vary over large spatial and time scales. Since 70.9% of the Earth is covered by oceans [1], it is easy to understand that satellite images represent a powerful tool to study the marine environment. Among satellite sensors, we can distinguish between active sensors, such as radars, and passive sensors, such as spectrometers. The former are composed of an electromagnetic radiation source which emits directed energy pulses, and of a collector, which measures the backscattered signal. The returns from these radars, given by the reflection of active signals from small gravity and capillary waves, can be formed into images of the sea surface, that display a large variety of surface phenomena at a high resolution, and under nearly all weather conditions. The latter measure solar radiation reflected by the Earth surface, and the emitted blackbody radiation. Both day light and a cloudless sky are needed for these measurements. As will be explained later on, from the intensity and frequency distribution of the radiation collected by passive sensors we can study the ocean colour, which is used to retrieve information about sea water constituents, sea bottom properties, and the presence of polluting substances or anomalous algae growth. For this reason, in the present thesis only passive optical sensor data will be considered.

The forerunner of ocean colour devoted satellite passive sensors was the Coastal Zone Colour Scanner (CZCS), launched by NASA in 1978. Since that date, a significant number of satellite sensors has been employed for studying the marine environment.

The importance given to EO missions can be understood by looking at Table 1 and Table 2, which list multi-spectral and hyper-spectral satellite sensors which are currently used for EO purposes by space agencies and by commercial satellite imagery providers.

Table 1:Current Earth Observation multi-spectral and hyperspectral sensors.

Sensor	**Agency**	**Satellite**	**Launch date**	**Swath (km)**	**Resolution (m)**	**Bands**	**Spectral Coverage (nm)**
AVHRR	NOAA (USA)	NOAA-18	20 May 2005	2900	1100	6	580-12500
AVNIR-2	JAXA (Japan)	ALOS	24 Jan. 2006	70	10	4	420-890
CHRIS	ESA (Europe)	PROBA	22 Oct. 2001	14	17 34	19 63	400-1050
COCTS	CNSA (China)	HY-1B	11 Apr. 2007	1400	1100	10	402-12500
CZI	CNSA (China)	HY-1B	11 Apr. 2007	500	250	4	433-695
ETM+	NASA (USA)	Landsat-7	15 April 1999	183	30 (60- thermal band)	7	450-12500
GOCI	KARI/KORDI (South Korea)	COMS	26 Jun. 2010	2500	500	8	400-865
HICO	NASA, ONR, DOD (USA)	JEM-EF Int. Space Stn.	18 Sep. 2009	50	100	124	380-1000
Hyperion	NASA (USA)	EO-1	21 Nov. 2000	7.75	30	220	356-2577
MERIS	ESA (Europe)	ENVISAT	1 Mar. 2002	1150	300/1200	15	412-1050
MODIS-Aqua	NASA (USA)	Aqua (EOS-PM1)	4 May 2002	2330	250/500/ 1000	36	405-14.385
MODIS-Terra	NASA (USA)	Terra (EOS-AM1)	18 Dec. 1999	2330	250/500/ 1000	36	405-14.385
MSC	KARI (South Korea)	KOMPSAT-2	28 July 2006	15	1	4	450-900
OCM	ISRO (India)	IRS-P4	26 May 1999	1420	360/4000	8	402-885
OCM-2	ISRO (India)	Oceansat-2	23 Sep. 1999	1420	360/4000	8	404-885
POLDER-3	CNES (France)	Parasol	18 Dec. 2004	2100	6000	9	443-1020
RSI	NSPO (Taiwan)	FORMOSAT-2	20 May 2004	24	2	4	450-900
SeaWiFs	NASA (USA)	OrbView-2	1 Aug 1997	2806	1100	8	402-885
TM	NASA (USA)	Landsat-5	1 Mar. 1984	183	30 (120-thermal band)	7	450-12500

Table 2:Current commercial Earth Observation satellites.

Satellite	**Company**	**Launch Date**	**Swath (km)**	**Resolution (m)**	**Bands**	**Spectral Coverage (nm)**
GeoEye-1	GeoEye	6 Sep. 2008	15.2	1.65	4	450-920
IKONOS	GeoEye	24 Sep. 1999	11.3	3.2	4	445-853
Orbview-2	GeoEye	1 Aug 1997	2800-1500	1130-4500	8	402-888
Quickbird	DigitalGlobe	18 Oct. 2001	16.5	2.4	4	450-900
SPOT-4	Spot Image	24 March 1998	60	20	4	500-1750
Worlview-2	DigitalGlobe	8 Oct. 2009	16.4	1.8	8	400-1040

1.2 Ocean colour remote sensing from optical sensors

Optical sensors measure solar radiation backscattered from the sea surface at several selected wavelengths. As mentioned before, radiation sources for these sensors are the Sun and the Earth. In particular, the spectrum of the solar radiation (Figure 1) is close to that of a black body with a temperature of about 5800 K, thus, the Sun mostly emits in the visible and near-infrared part of the spectrum (0.4-0.7 μm) while the Earth, being at a mean surface temperature of about 280 K, emits mostly in the thermal infrared part of the spectrum (8-14 μm). Optical sensors for remote sensing of the ocean colour employ wavelengths in the visible and near- infrared, thus Earth emitted radiation can be considered as negligible.

However, the photons from the sun can follow different pathways before they reach the sensor. In particular, we can consider the following main contributions to the remotely-sensed signal (see Figure 2):

- path radiance: light reaching the sensor after scattering of photons by the atmosphere;
- direct radiance: light reaching the sensor after specular reflection of direct sunlight at the sea surface;
- water leaving radiance: light upwelling from the sea surface after back-scattering in water.

In addition, we can note that light is also attenuated due to atmospheric absorption and scattering while going through the optical path from the source to the sensor.

It is only the upwelling water leaving radiance that carries any useful information on the water body, while atmospheric contribution and specular reflection at the sea surface represent noise sources, and must be corrected for. In particular, attenuation due to atmospheric absorption and scattering cannot be prevented during the remote measurement process, thus, the upwelling radiance from the water has to be processed by means of some atmospheric correction algorithm, in order to identify what the water leaving radiance contribution would have been if there were no atmosphere in between the sensor and the water body. Atmospheric correction represents an important issue for analytic approaches [2], since these algorithms need some initial estimate of many parameters characterizing those atmospheric components which contribute to absorption and scattering of light. Such parameters must be determined using other sources of information, like in-situ measurements. However, for many cases these measurements could not be available.

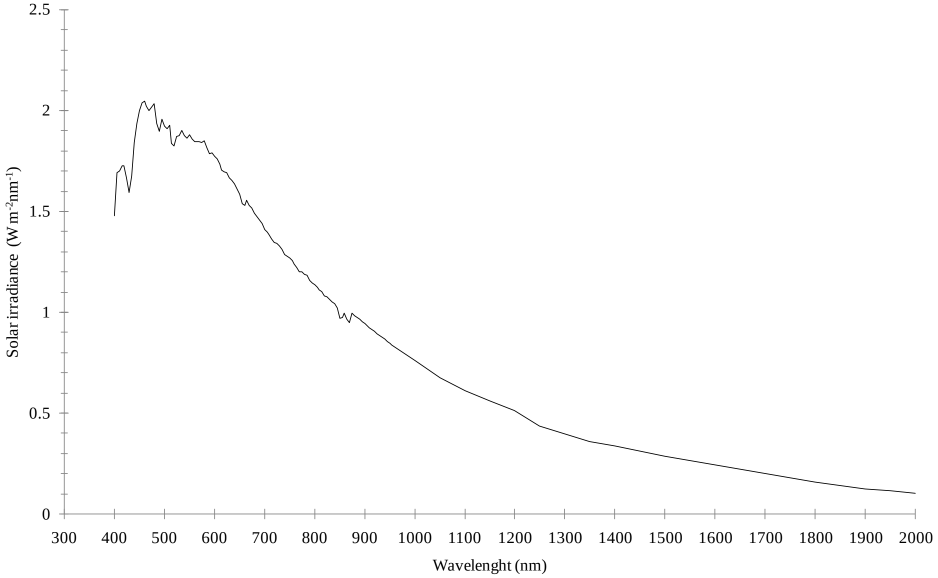

Figure 1: Measured extraterrestrial solar spectral irradiance at mean Earth-Sun distance. Plotted from data in [3].

Looking in more detail at the water leaving radiance contribution, we can identify many factors affecting the signal. Direct sun light and diffuse sun light (that is sunlight scattered by the atmosphere) penetrating under the sea surface may be absorbed or scattered by water molecules, or by the various suspended and dissolved materials present in the water. Part of this light may reach the sea bottom (in shallow waters), and be reflected from it. At the end, part of the reflected radiation and part of the scattered radiation will reach the remote sensor. The remaining part will be scattered towards other directions, or it will be absorbed while going up.

Because of these processes, the signal collected by the remote sensor carries information on the type and concentration of substances present in water, together with bottom properties. In order to analyse the remotely sensed signal, it is important to understand how solar radiation interacts with the sea water body, and how the optical properties of sea water are modified by the presence of different types of marine constituents. In this framework, the effect of pure sea water, which is sea water in absence of any organic or inorganic matter other then water molecules and dissolved salts usually present in oceanic water, is usually distinguished from the effect of particulate, which can be classified into three main components [4] [5]:

- Phytoplankton: the autotrophic component of plankton. They are able to carry out the photosynthetic process, thanks to the chlorophyll content within their cells. Other microscopic organisms are also included in this contribution.
- Suspended matter: suspended inorganic sediments.
- Yellow substance: coloured dissolved organic matter (CDOM). This contribution also includes detritus which have absorption characteristics similar to those of yellow substances.

In addition, we have to consider bottom contribution, which can influence the remotely sensed ocean colour in cases where the water is sufficiently clear and shallow. This contribution depends on depth, water transparency, and bottom type. The latter could be, for instance, sandy, rocky, coraline or algae covered.

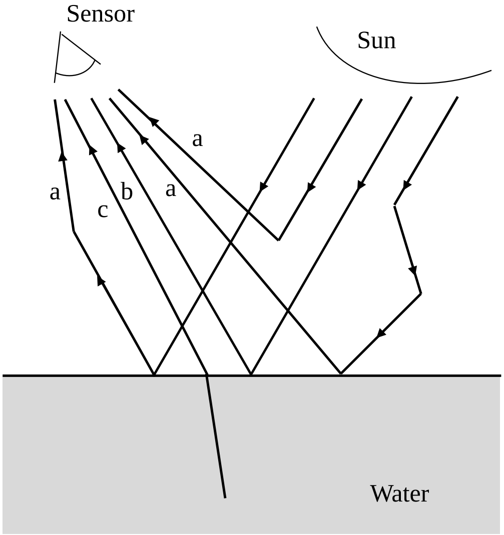

Figure 2: Contributions to the remotely sensed signal. (a) Light scattered by atmosphere. (b) Specular reflection of direct sunlight at the sea surface. (c) Water leaving radiance.

Moreover, in the literature a distinction is usually made [6] [3] between Case 1 waters , which are those where phytoplankton contribution dominates and is the principal responsible for variations in water optical properties, and Case 2 waters, which are those waters where also suspended matter and yellow substance contribute.

The ocean colour is thus determined by scattering and absorption of visible light by pure water itself, as well as by the inorganic and organic, particulate and dissolved, material present in the water. The following paragraph reports a description of how these processes affect the remotely sensed signal.

1.3 Ocean colour

The observed ocean colour is a direct consequence of the interaction of incident light flux with water molecules and with other organic and inorganic substances present in it. Spatial and time variations in water composition are then reflected in colour variations.

In order to interpret the ocean colour, it is useful to express the remotely detected signal as a function of concentrations of the various substances present in the water column. The following paragraphs define the link between radiometric quantities, which can be measured by remote sensors, and water constituent concentrations.

1.3.1 Radiometric quantities

1.3.1.1 Geometry

Figure 3 shows the geometry of the problem. Polar spherical coordinates are used, so that a generic direction of light propagation, identified by a versor $\hat{\xi}$, is expressed in terms of the zenith angle θ, between the direction of light propagation and the upward perpendicular to the horizontal reference plane, and the azimuth angle ϕ, the angle between the vertical plane containing the light beam, and a specified vertical reference plane, usually chosen so as to simplify calculations. Here, according to the formulation used in [7] [8], the direction of zero azimuth is defined as the position of the sun.

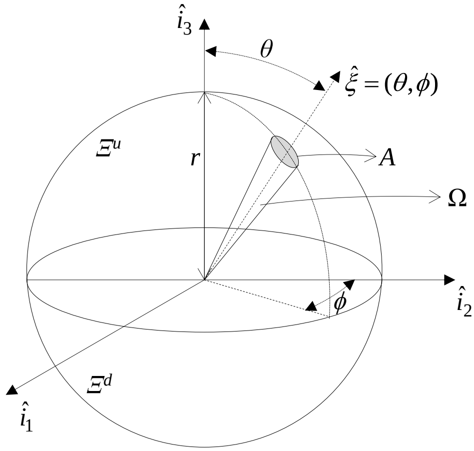

Figure 3: Definition of the polar angles and of the upward (Ξ^u) and downward (Ξ^d) hemispheres. $\hat{\xi}$ represents the versor identifying a direction determined by the angles θ and ϕ.

In Figure 3 the concept of solid angle is also represented: considering the area A on the surface of the sphere of radius r in figure, the solid angle, Ω, in units of steradians (sr), is the set of directions defining this area so that $\Omega = A/r^2$.

1.3.1.2 Radiant flux, radiance, irradiance

Radiant flux Φ can be defined as the radiant energy per unit time, $\Delta Q/\Delta t$, emitted by a point source (or by an infinitesimally small element of an extended source). Thus the *radiant intensity* is defined as:

$$I = \frac{\Delta \Phi}{\Delta \Omega} = \frac{\Delta Q}{\Delta t \Delta \Omega} \tag{1}$$

If we have an extended source it is necessary to consider the size of the area from which light is emitted or reflected. *Radiance L* is defined as the radiant intensity per unit area of a plane at right angles to the direction of light flow, $L = dI/dA$. *Surface radiance* is the radiant flux emitted in a given direction $\xi = (\theta, \phi)$ per unit solid angle, per unit projected source area. When the direction is not perpendicular to the source area A_s, the projected source area is $A_s \cos\theta$ (Figure 4). *Field radiance* at a point in space, in direction ξ, is the radiant flux in an element of solid angle $d\Omega$, centred on ξ, passing through the infinitesimal area dA at right angles to ξ. The field radiance at a point in a plane surface surrounded by an infinitesimal area, dS, is the radiant flux through the projected surface area, $dS \cos\theta$. *Spectral radiance*, $L(\theta, \phi, \lambda)$ is radiance per unit wavelength, either passing a point in space (spectral field radiance) or emitted by an extended source (spectral surface radiance).

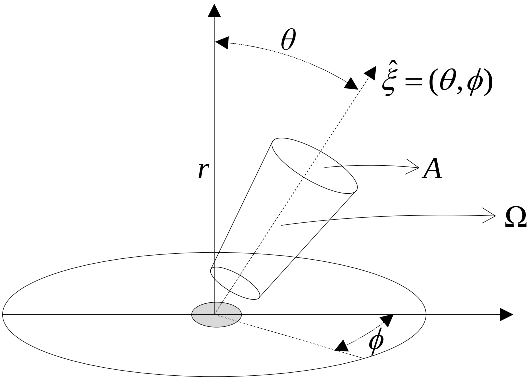

Figure 4: Surface radiance definition.

An operational definition of spectral radiance is the following:

$$L(\theta, \phi, \lambda) = \frac{\Delta Q}{\Delta t \Delta A \Delta \Omega \Delta \lambda} \quad (\mathrm{W\ m^{-2}\ sr^{-1}\ nm^{-1}}) \tag{2}$$

that is, the radiant energy ΔQ measured over the integration time Δt, by a sensor with detector area ΔA, angular field of view $\Delta\Omega$, and bandwidth $\Delta\lambda$ centred on λ. The measured spectral radiance is equivalent to the radiance emitted in the direction of the sensor by an extended source of area A_s, equal to the instantaneous field of view (IFOV), represented in grey in Figure 5. In particular, the radiant flux intercepted by the sensor is obtained by integrating the contributions of all infinitesimal area elements dA_s, contained within the

IFOV, each contribution being proportional to the infinitesimal area times the cosine of the nadir viewing angle θ, whose variations within the area will be negligible for a sensor with a narrow angular field of view.

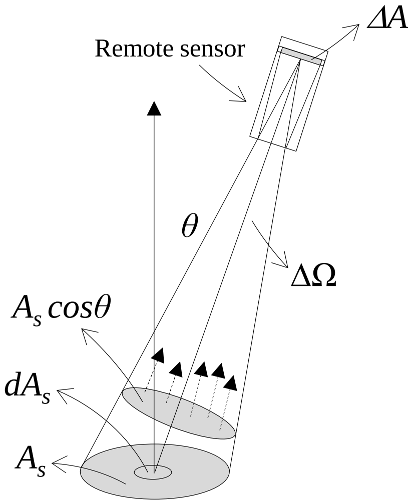

Figure 5: Measurement of the spectral radiance emitted by an extended horizontal source.

In order to measure $L(\lambda)$ with a good resolution in all involved parameter domains, without encountering effects like diffraction, the intervals Δt, ΔA, $\Delta\Omega$ and $\Delta\lambda$ must be small enough. In practice, there is usually a tradeoff between the different parameters.

Using the definition of radiance we can also define the concept of irradiance. *Plane irradiance* is the total radiant flux per unit area incident on an infinitesimal element of a plane surface, divided by the area of that element and integrated with respect to solid angle:

$$E(\lambda) = \int L(\vartheta, \phi, \lambda) |\cos\theta| d\Omega \quad (\mathrm{W\ m^{-2}\ nm^{-1}}) \tag{3}$$

The $\cos\theta$ term indicates that the contribution by radiance from different directions is weighted by the cosine of its zenith angle. When all directions are treated equally, we obtain the s*calar irradiance*, E_0, that is the integral of the radiance distribution at a point over all directions about this point:

$$E_0(\lambda) = \int L(\vartheta, \phi, \lambda) d\Omega \quad (\mathrm{W\ m^{-2}\ nm^{-1}}) \tag{4}$$

By integrating E over the upper and lower hemispheres we obtain the *downwelling (plane) irradiance*, E_d, and *upwelling (plane) irradiance*, E_u, which are the irradiances incident on a horizontal surface respectively from the upper hemisphere Ξ_d (where the light is travelling downward), and the lower hemisphere Ξ_u (where the light is travelling upward):

$$E_d(\lambda) = \int_{\Xi_d} L(\vartheta, \phi, \lambda) |\cos\theta| d\Omega \quad (\mathrm{W\ m^{-2}\ nm^{-1}}) \tag{5a}$$

$$E_u(\lambda) = \int_{\Xi_u} L(\vartheta, \phi, \lambda) |\cos\theta| d\Omega \quad (\mathrm{W\ m^{-2}\ nm^{-1}}) \tag{5b}$$

Of course we can also define the upwelling and downwelling scalar irradiances:

$$E_{0d}(\lambda) = \int_{\Xi_d} L(\vartheta, \phi, \lambda) d\Omega \quad (\mathrm{W\ m^{-2}\ nm^{-1}}) \tag{6a}$$

$$E_{0u}(\lambda) = \int_{\Xi_u} L(\vartheta, \phi, \lambda) d\Omega \quad (\mathrm{W\ m^{-2}\ nm^{-1}}) \tag{6b}$$

Downwelling and upwelling irradiances may be measured with a cosine collector, (angular field of view 180^{o}) that measures the light falling on the surface of a flat diffuser, and is thus sensitive to light from different directions, in proportion to the cosine of the incidence angle. Thus, an operational definition of downward and upward spectral irradiance is the light incident on the detector area ΔA of a horizontal cosine collector, with spectral bandwidth of $\Delta\lambda$, over the integration time Δt, and pointing, respectively, downward or upward:

$$E_d(\lambda) = \frac{\Delta Q_d}{\Delta t \Delta A \Delta \lambda} \quad (\mathrm{W\ m^{-2}\ nm^{-1}}) \tag{7a}$$

$$E_u(\lambda) = \frac{\Delta Q_u}{\Delta t \Delta A \Delta \lambda} \quad (\mathrm{W\ m^{-2}\ nm^{-1}}) \tag{7b}$$

Alternatively, downwelling irradiance may be measured using a Lambertian reference panel, that is. a panel with a surface which reflects radiance equally in all directions regardless of incidence angle. The radiance distribution reflected into the upper hemisphere from an ideal Lambertian panel would thus be isotropic. After correction for panel reflectivity, the downwelling irradiance may be obtained by multiplying the radiance reflected from the panel by π (this arises from the definition of irradiance in equation (5a)).

Regarding total scalar irradiance, measurements can be performed by recording the light incident on the surface of a diffusing sphere, which is equally sensitive to light from all directions, while upwelling and downwelling scalar irradiances may be recorded by shading the sphere from upper and lower hemisphere light, respectively.

1.3.1.3 Average cosines

A simpler way of specifying the angular structure of the light field is by determining its average cosines. The *average cosine* for the total light field is equal to the net downward plane irradiance divided by the scalar irradiance:

$$\bar{\mu}(\lambda) = \frac{E_d(\lambda) - E_u(\lambda)}{E_0(\lambda)} \tag{8}$$

The *downwelling average cosine* and the *upwelling average cosine*, are respectively defined as

$$\bar{\mu}_d(\lambda) = \frac{E_d(\lambda)}{E_0(\lambda)} \tag{9a}$$

$$\bar{\mu}_u(\lambda) = \frac{E_u(\lambda)}{E_0(\lambda)} \tag{9b}$$

1.3.2 Apparent Optical Properties

Apparent optical properties (AOPs) are those optical properties of the water body which are influenced by the angular distribution of the light field, as well as by the types and concentrations of substances present in the water [9]. These properties are obtained from measurements of radiance or irradiance. In addition to the AOPs, inherent optical properties (IOPs) have also been defined [9]. These are independent of the angular distribution of the light field, and are determined exclusively by the properties of the water body, that are the types and concentrations of water constituents. The main AOPs used in remote sensing of the oceans will now be introduced, while IOPs will be discussed in Section 1.3.3.

1.3.2.1 Reflectance, remote sensing reflectance

For ocean remote sensing applications, *reflectance* is defined as the ratio between the upwelling and downwelling irradiances at a certain depth z:

$$R(z,\lambda) \equiv \frac{E_u(z,\lambda)}{E_d(z,\lambda)} \tag{10}$$

For measurements taken above the sea surface, it is commonly used the *spectral remote sensing reflectance*, R_{rs}, defined as the ratio between upwelling, directional spectral radiance and downwelling plane irradiance:

$$R_{rs}(z,\vartheta,\phi,\lambda) \equiv \frac{L(z,\lambda)}{E_d(z,\lambda)} \quad (\mathrm{sr}^{-1}) \tag{11}$$

computed either immediately above the sea surface, $z=0^+$ [10] or immediately below the surface, $z=0^-$ [7] [8]. The remote sensing reflectance is a measure of how much of the downwelling light that is incident onto the water surface is eventually returned through the surface, in direction (θ, ϕ), so that it can be detected by a radiometer pointed in the opposite direction.

1.3.2.2 Diffuse attenuation coefficient

Diffuse attenuation coefficient for downwelling irradiance (K_d) defines the rate of decrease of downwelling irradiance with depth:

$$\frac{dE_d(z,\lambda)}{E_d(z,\lambda)} = -K_d(\lambda)dz\,. \tag{12}$$

By integrating both sides of equation (12) we obtain the following:

$$\ln\frac{E_d(z,\lambda)}{E_d^i(\lambda)} = -K_d(\lambda)\,z \tag{13}$$

where $E_d^i(\lambda) = E_d(z=0,\lambda)$, that is:

$$E_d(z,\lambda) = E_d^i(\lambda)\,e^{-K_d(\lambda)\,z} \tag{14}$$

thus, attenuation of light travelling in the water body from depth 0 to depth z follows an exponential law. This is actually true for a generic homogeneous medium, and is the basis for radiative transfer theory in atmosphere and in water.

Besides the diffuse attenuation coefficient for downwelling irradiance, the diffuse attenuation coefficient for upwelling irradiance (K_u) and for scalar irradiance (K_0) can analogously be defined. These coefficients are strongly correlated to the inherent optical properties of the water and also to other AOPs, such as reflectance.

1.3.3 Inherent Optical Properties

As anticipated in Section 1.3.2, inherent optical properties (IOPs) are determined by the types and concentrations of water constituents, and are not influenced by the angular distribution of the incident radiation field. The principal responsible for the fate of radiation entering the water body, and thus for the ocean colour, are *absorption* and *scattering* processes, that are described by means of some IOPs. Absorption removes photons from the light beam. These photons bring the absorbing molecules to higher energy levels. Scattering, on the other hand, make photons change their direction when impinging on molecules. In particular, we can distinguish between elastic scattering, which happens when the scattered photon has the same wavelength as the incident one, and inelastic scattering, which implies a change in the wavelength of the scattered photon. Among inelastic processes, we can mention Raman scattering by water molecules and induced fluorescence emission from CDOM and phytoplankton.

Considering natural sunlight in the visible part of the spectrum (roughly between 400 nm and 700 nm) as the only radiation incident on the water surface, the colour of the ocean is determined by scattering and absorption processes. In this context, the IOPs of relevance are the *absorption coefficient* (a, dimensions of [m^{-1}]), which determines the exponential rate of decay of flux per unit pathlength of light in the medium, and per unit incident flux, due to absorption, and the *scattering coefficient* (b, dimensions of [m^{-1}]), which defines, analogously, the rate of decay of the flux due to scattering. In particular, scattering coefficients for elastic and inelastic processes must be defined separately.

It is important to note that both absorption and scattering coefficients are defined for a collimated, monochromatic flux, incident normally on the medium, and passing through an infinitesimally thin layer of the medium. They are not determined for natural conditions of illumination, as apparent optical properties are. Since AOPs, like reflectance, are usually measured using flat plate collectors facing downwards and upwards, with the angular distribution of the incident flux on the collectors being determined by environmental conditions, the relationships between inherent and apparent optical properties typically depend on the angular distribution of the light field under which apparent properties are measured. Hence, when linking IOPs and AOPs it is usually necessary to have a description of the angular distribution of the light field, which can be given by downwelling average cosine and upwelling average cosine, defined in (9a), (9b).

Because IOPs are not influenced by illumination conditions, they also have the advantage of being additive. More precisely, in a complex medium, composed of many different constituents, the contributions of individual constituents to an IOP can be summed together. This property is not valid for AOPs. Thus, scattering and absorption coefficients due to phytoplankton, CDOM, yellow substance and pure water are summed to obtain the absorption and scattering coefficients of Case 1 and Case 2 waters.

In Case 1 waters the dominant contribution is due to phytoplankton, so that other contributions co-vary with phytoplankton. Case 2 waters are more complex, and different contributions must be considered separately.

In particular, the contributions of each component to an IOP can be expressed in terms of the specific IOP of each component, that is, the IOPs per unit concentration of the component. Hence, the total absorption coefficient can be expressed as the product of the concentration of each substance and a corresponding specific absorption coefficient:

$$a = a_w + P \cdot a_p^* + Y \cdot a_y^* + S \cdot a_s^* \quad (\mathrm{m}^{-1}) \qquad (15)$$

where a_w is pure sea water absorption coefficient, a_p^*, a_y^* and a_s^* are the specific absorption coefficients for phytoplankton, yellow substances and suspended matter (in units of m^2/g), and P, Y, S are the corresponding component concentrations (in units of $\mathrm{g/m}^3$).

Backscattering coefficient can be treated analogously, assuming that yellow substances, being dissolved, do not contribute significantly to scattering:

$$b_b = b_{bw} + P \cdot b_{bp}^* + S \cdot b_{bs}^* \quad (\mathrm{m}^{-1}) \qquad (16)$$

The above relations allow to link the inherent optical properties of natural sea water to the concentrations of its constituents.

1.3.4 Relation between ocean colour and IOPs

Remote sensing measurements of the sea surface consist in a set of radiance or reflectance values which represent the apparent optical properties of the water body, and which also include the effect of light passing through the atmosphere. The number of available radiances or reflectances depends on the number of spectral bands of the sensor.

Ocean colour algorithms transform the set of radiances/reflectances into the values of constituent concentrations. In shallow waters the bottom effect must be also considered, thus water depth and bottom type represent additional unknowns.

Modelling the ocean colour means finding the relation between ocean colour and IOPs, and this implies that two issues must be faced:

- developing theoretical models which represent reflectance as a function of the specific IOPs;
- classifying the spectral behaviour of the specific IOPs of water constituents, also considering variability in water composition.

These issues make analytic modelling a difficult task. The following chapter describes possible approaches to the study of the remotely sensed ocean colour.

Chapter Two: Information extraction methods for remotely sensed images

The study of the ocean colour can be used to retrieve concentrations of sea water constituents, water depth, bottom properties, or to detect pollutants. Many efforts have been made to develop techniques for information extraction from the remotely sensed ocean colour signal. However, without regard to the particular application, we can distinguish between two big branches of techniques: those relying on a Bayesian modelling approach, and those exploiting computational intelligence. The former try to develop a theoretical model of the water body under examination, and necessarily need to make some hypothesis on water composition, bottom effect, and atmosphere composition. Depending on the target quantity to be retrieved, also some measurements are needed. The number of these measurements depends on the water type (Case 1 or Case 2) and on the number of available bands. The latter do not make any hypothesis, but they use significant datasets of measurements of target quantities to be retrieved. When such a dataset is not available, simulated data can be used, exploiting some theoretical bio-optical models. In this case, the resulting approach will be a mixture of model-based and computational intelligence-based approaches.

2.1 Analytical methods

The simplest approach for retrieving water optical properties and/or water column depth from multi-spectral data is represented by regression methods, which derive the unknown properties from a number of measurements taken on site. These are called empirical methods, and their results are limited to specific case studies. More precisely, empirically derived relationships are valid only for data having statistical properties identical to those of the data set used for the determination of coefficients. These algorithms are thus particularly sensitive to changes in the composition of water constituents.

Model-based approaches aim to determine the relationship between the inherent and apparent optical properties of the water column. Among model-based approaches, we can distinguish between analytical modelling and radiative transfer modelling. Radiative transfer numerical models (e.g., Hydrolight [10] [11]) compute radiance distributions and related quantities (irradiances, reflectances, diffuse attenuation functions, etc.) in the water column as a function of the water absorption and scattering properties, the sky and air-water interface conditions, and the bottom boundary conditions. An analytical model is a simplification of the full radiative transfer equations, based on a set of given assumptions. Analytical models have the advantage that, due to their relative simplicity, they can be solved quickly. This is important in remote sensing applications, where a model must be evaluated at every pixel of an image.

If an analytical approach is followed, there are two ways to find the desired optical properties. The first one is represented by semi-empirical methods, which give direct or explicit estimates of target quantities. The second one is represented by implicit methods based on nonlinear optimization, which minimize the difference between calculated and measured reflectance by varying input variables. Calculated radiance can be obtained either by means of analytical models (semi-empirical models) or radiative transfer models.

2.1.1 Semi-empirical methods

Semi-empirical methods use analytic expressions to relate apparent optical properties and water properties. In particular, two steps are followed: first an ocean colour semi-analytical model is implemented, then algebraic expressions are derived that relate ocean colour to the target quantities to be retrieved. A semi-analytical model is built using empirical data of the inherent optical properties, and of the concentrations of individual water components. Starting from these data, expressions relating optical properties and water components are derived, and a theoretical model is obtained. The model is then simplified, to reduce the number of unknowns, making use of approximations, or of the inter-dependencies between unknowns. The result is a set of algebraic equations that can be solved sequentially, starting from remotely sensed apparent optical properties, to obtain each of the unknown components of the model [5]. Examples of this approach can be found in [12] [13] [14]. If relationships are nonlinear, solutions may be found either by using look-up tables (in which results from multiple runs of the theoretical model are stored) or by means of bisection methods for reducing differences between predictions and observations.

The advantage of this approach is that it makes use of the known optical properties for specific components, and couples them with theoretical models of remote sensing reflectance. Although there are errors associated with the measurements used in the empirical relationships, the results appear quite accurate when applied to specific cases [12] [13]. Moreover, as stated before, these methods allow to quickly find the solution. On the other hand, one of the disadvantages is caused by the fact that empirical relationships, derived from measured data, tune the model to the specific regions where measurements have been taken. In other words, this approach gives accurate results when applied to specific cases, but has a limited generalization capability when the estimate is extended to different regions. Moreover, such methods can be implemented only with a limited number of unknown model parameters and variables (e.g. concentrations to be retrieved).

2.1.2 Implicit methods

A more refined approach with respect to semi-empirical methods is represented by the inversion of remotely sensed radiances, based on nonlinear optimization. In particular, a forward model for radiances at water level (which is usually a semi-analytical model) is inverted by minimizing the differences between the calculated values and the measured radiances. In particular, measured radiances undergo an atmospheric correction procedure, in order to be compared to calculated radiance at water level. The minimization can be performed using many different methods, but the basic concept which guides all these techniques is the search for the minimum difference between two spectral curves: the theoretical radiance and the remotely sensed radiance. More precisely, the χ^2 of difference between modelled and measured radiances is minimized by iteratively changing the input parameters for the forward model. The χ^2 is defined as:

$$\chi^2 = \sum_{\lambda} \left(L_{sat} - L_{model}\right)^2 \quad (17)$$

where L_{sat} represents radiance measured from satellite sensor at water level, L_{model} represents theoretical radiance obtained by the model, and the sum is taken over all wavelengths λ. In particular, theoretical radiance can also be obtained by means of radiative transfer calculations, which, however, require a substantial computation time. A certain threshold is usually set to terminate the iterative minimization procedure. The input set of variables corresponding to the minimum represents the desired solution. Thus, water and bottom properties are simultaneously retrieved.

Nonlinear optimization techniques, together with model-based approaches have been widely used for ocean colour applications. In particular, analytical model inversions have been applied to the retrieval of water quality variables from airborne hyperspectral imagery [15] [16]. In [17] five water column and bottom properties (chlorophyll, dissolved organic matter, and suspended sediments concentrations, bottom depth, and bottom albedo) have been estimated by means of a Levenberg-Marquardt optimization method, using a remote sensing reflectance airborne hyperspectral dataset. In [18] a matrix inversion method has been used to retrieve water component concentrations.

These implicit methods are capable of reproducing the nonlinear nature of the modelled environment, and, once a forward model is adopted, they do not need any in-situ measured data. Most of implicit methods are based on a widely accepted model, proposed by Sathyendranath, Prieur, and Morel in [19], where sub-surface spectral reflectance is expressed in terms of absorption and backscattering coefficients. However, an underlying assumption of the optimisation methods is that the forward model is representative of the natural environment. This assumption, and thus the forward model choice, brings to a systematic error, which cannot be eliminated, nor it can easily be estimated. Generally speaking, all methods that are based on bio-optical models are affected by this systematic error. Other sources of errors are due to noise in satellite data, which however, unlike systematic errors due to model choice, appear in all methods.

Besides the disadvantage represented by systematic errors, several aspects of this techniques require attention during implementation. In particular, the parameterisation of the forward model should be carefully chosen, so as to ensure that the unknowns are as independent of each other as possible, otherwise ambiguities could arise in the estimation of desired quantities. An adequate selection of the initial guess is also of prime importance. This can be achieved by means of empirical algorithms, or by using the value from the adjacent pixel. Moreover, since multiple minima of the χ^2 could bring multiple solutions, it is appropriate to set upper and lower limits for each quantity to be retrieved. This also contributes in reducing computation time, which however remains high.

Last, but not least, atmospheric correction represents an important issue, since estimates of many parameters, characterizing atmosphere composition, are needed in order to account for absorption and scattering of light, during the optical path between water level and sensor quote.

2.1.3 Principal component approach

All previously described approaches necessitate of an atmospheric correction to obtain water-leaving radiances. An alternative solution is represented by an integrated approach, in which the optical properties of the atmosphere are taken to be additional variables in an inversion problem [5]. Top of the atmosphere (TOA) radiances, measured by a satellite sensor, are the starting point for this inversion method. Target quantities are usually water component concentrations, bottom properties, as well as atmospheric parameters. Besides atmospheric correction, an additional issue to be considered is the high correlation between signals from different bands in Case 2 waters ocean colour data.

To address both issues, algorithms based on inverse modelling of the sea-atmosphere system through principal component multilinear regression, have been developed [20], in which the nonlinearity is managed by a piecewise-linear approximation. The main difference with respect to the previously described implicit methods is that the inverse model is not based on physical considerations: these are only used in the forward model, which is usually the one in [19]. The basic idea is to find a piecewise-linear map between a set of spectral TOA radiances and a set of geophysical quantities. In order to deal with the high correlation between signals from different wavebands, principal component analysis (PCA) can be exploited [21] [22]. Radiative transfer modelling is used to generate data sets of TOA radiances, corresponding to given variations of water constituents and atmospheric properties. Then, PCA of the simulated data is used to determine the spectral dimensionality of the data, and the weighting of each spectral channel required to retrieve the geophysical variables of interest. This approach accounts for the correlation between signals in different spectral channels, and improves reconstruction accuracy of retrieved constituents, giving better results than using subsets of the available wavebands. Principal components offer an orthogonal representation of the data, which allows the multivariate inversion, that would be hard to do with original radiances, due to high spectral correlation. A linear estimation formula is then derived to compute the geophysical variables from TOA measurements:

$$\hat{p}_i = \sum_{j=1}^{n} k_{ij} L_j + A_i \tag{18}$$

where $\hat{p}_i$ is an estimate of the target geophysical variable, j is the measurement channel number, from 1 to n, where n is the number of spectral channels in the instrument, k_{ij} is the weighting coefficient of channel j for variable i, L_j is the measured radiance in channel j, and A_i is the offset value for variable i. By applying the method to TOA radiances, the atmospheric influence is implicitly taken into account. This approach relies on the fact that the application of an explicit atmospheric correction does not increase the information content with respect to water constituents and bottom properties. Although atmospheric scattering has a major influence on satellite data, these data also contain all signal variations caused by water constituents. Thus, signal variations that are not resolved in TOA data, cannot be resolved after atmospheric correction either.

The approach briefly described in this paragraph has the advantage of being a very simple, stable algorithm, which can be rapidly implemented even for large scenes, without convergence problems typical of iterative inversion techniques. It also solves the problems related to high correlation and atmospheric correction. However, systematic uncertainty due to forward model choice still lasts. Moreover, the main limitation is due to the nonlinearity of the dependence between the optically significant substances and the radiances. To overcome these limitations computational intelligence techniques must be used.

2.2 Computational intelligence based methods

Computational intelligence techniques allow building a mapping from a set of input variables (e.g. TOA spectral radiance values, measured by a satellite sensor) to some output set of quantities (e.g. sea water parameter concentrations, bottom depth etc…). These techniques are able to represent nonlinear relationships between input and output quantities, and do not rely on any assumption or model choice. Not being affected by systematic errors, related to bio-optical models, computational intelligence techniques represent a valid alternative to model-based techniques. Moreover, the low computation time allow to easily process big remotely sensed images.

However, these are supervised techniques, therefore, a consistent dataset of input and target measured variables is needed to train an algorithm and build the mapping. The training dataset must be an exhaustive and representative set of the possible conditions the trained algorithm will be called to face in the application. Since in many cases such a dataset cannot be collected, simulated data, obtained by means of a forward theoretical model, are often used for training. For ocean colour applications the bio-optical model by Sathyendranath, Prieur, and Morel [19] is usually adopted.

Provided that a training dataset has been built in an appropriate way, and that overlearning has been avoided during the training phase, these techniques allow to achieve accurate results, and, more importantly, they have generalization capabilities.

The following paragraphs show some examples of computational intelligence techniques which have been used in the analysis of remotely sensed optical images, for applications in the retrieval of optically active constituents, or in the estimation of bottom properties and water depth.

2.2.1 Neural networks

An artificial neural network is a parallel computing architecture that can be trained by supervised learning to perform nonlinear mappings. It can be regarded as a black-box model, which is able to represent the nonlinear relationships between input and output variables, any time a new input set is under examination, having learned from the examples which have been considered during the training phase. Such a network is made of a set of nodes, which are called neurons, eventually organized in layers, and connected together. Neurons represent the processing units of the neural network. The processing conducted by neurons consists in forming a weighted sum of the inputs, followed by a nonlinear transfer function to produce the output. The outputs of one layer become the inputs to the next layer in the network. Proper weights are established by supervised learning, using input data vectors with known desired outputs. Neural networks will be described in more detail in Section 3.1.

A neural network approach has often been used in the ocean colour inverse problem, which involves inversion of the relationships between reflectances in different spectral bands, and the concentrations of multiple types of water constituents. In these cases the neural network is used as a multiple nonlinear regression technique. In complex Case 2 waters, containing pigments, yellow substances and suspended particulate material, the reflectance in a band depends on more than one variable, thus, simple linear regression is not sufficient for retrieving the concentrations of water constituents. In particular, for a limited range of concentrations multiple linear regression could be used, but, when higher ranges of concentrations have to be considered, nonlinear regression techniques must be used. In such cases, the neural network approach results to be an efficient and simpler approach. Regression by means of a neural network can be performed either starting from a set of measurements (i.e. concentrations and reflectances), or from a set of simulated reflectances, obtained exploiting a theoretical bio-optical model. In particular, in this case, a forward model is used to build a dataset of reflectances (or TOA radiances) for training the network, starting from a set of water constituent concentrations. Then, the trained network is adopted as an inversion technique to retrieve the desired concentrations from measured reflectances (or TOA radiances). If TOA radiances are used, atmospheric correction is implicitly considered, otherwise atmospheric parameters must also be known. Performance evaluation then requires the presence of an additional dataset, different from the training set, to be used for testing the network and for evaluating its generalization capabilities.

Many examples of a neural network approach combined with a forward model can be found in the literature [23], ranging from generalized radial basis function (RBF) neural networks for the estimation of concentrations of phytoplankton, non-chlorophyllous particles and yellow substances in Case1, Case 2 and mixed Case1 and 2 waters [24], to multi-layer perceptron (MLP) neural networks [25], used for the retrieval of spectral absorption coefficients of CDOM and non-pigmented particulate matter. In [26] a comparison between RBF and MLP neural networks has also been presented for the estimation of water optically active constituents in Case 2 waters.

The performance of a neural-network-based method is determined by the goodness of training set, which must be representative of the environment in which the network is asked to operate, and must have an adequate size with respect to the number of inputs and coefficient involved in the network. If simulated data are used, then performance depends on the model used to produce data, which must describe as accurately as possible the optical properties of the water constituents, their variability, and the radiative transfer. If attention is paid to dataset requirements, results are much more accurate than those achieved by multilinear techniques (mean square error is reduced by two order of magnitude [24]) and allow to reproduce the strong nonlinearities which characterize Case 2 waters.

However, if a dataset of measured values can be collected, in this case results will not be affected by model accuracy. An example of a neural network approach for bathymetry estimation, using a dataset of remotely sensed spectral radiances measured by the AVIRIS airborne sensor, is reported in [27]. In this study the authors implicitly consider atmospheric correction by including additional bands as input nodes, in order to provide the network with atmospheric information.

2.2.2 Fuzzy systems

The use of fuzzy logic-based systems is appropriate in problems related to real world modelling, where ambiguities and uncertainties can be faced by describing the problem using linguistic variables, instead of classical variables, so that the description results more intuitive and interpretable than a pure mathematic one. Fuzzy logic [28] is an extension of classical logic based on the use of fuzzy sets, that are classes of objects with a continuum of grades of membership. In practice, in most cases a fuzzy logic system performs a nonlinear mapping of inputs into outputs, by means of linguistic expressions.

Fuzzy systems are composed of a set of rules, each one being a conditional statement, expressed in terms of linguistic variables and fuzzy sets, where fuzzy sets characterize the involved variables. Each rule produces a consequence, and, finally, all the obtained consequences must be aggregated, in order to obtain a unique conclusion, that is the output.

The fuzzy set partition, which describes the input variable behaviour and variability, and the rules, which compose the inference system, can be set basing on some expert's previous knowledge, or they can be determined by means of specific algorithms, which exploit a training dataset. The first approach implies a big human effort and a deep pre-existing knowledge of the phenomena to be modelled. Thus, usually the set of fuzzy rules is directly derived from the dataset.

Regarding the dataset, the same considerations done for neural networks hold. In particular, training dataset can be built using both measured or simulated data.

As an example of the use of fuzzy systems for ocean colour applications, in [29] the authors use a fuzzy inference system to solve the inverse problem of retrieving chlorophyll concentration, non-chlorophyllous particle and yellow substance absorption coefficients, from subsurface spectral reflectance. In particular, basing on the forward model by Sathyendranath, Prieur, and Morel [19], the authors build a simulated training dataset, composed of triplets of values of the above mentioned optical properties and the corresponding reflectance values. This simulated dataset is then used to determine the structure of the system, which is then optimized by means of a genetic algorithm.

Another example of the application of fuzzy logic-based systems to the ocean colour inverse problem is reported in [30], where the authors build a multi-objective evolutionary optimization of an Adaptive Network-based Fuzzy Inference Systems (ANFIS), for the same inverse problem faced in [29], using the same simulated dataset. As Section 3.2 will describe, ANFIS combine the advantages of fuzzy systems with those of neural networks, showing both interpretability and adaptability.

2.2.3 Genetic algorithms

Genetic algorithms (GAs) for the retrieval of water constituent concentrations and optical properties have only been used in a model-based scheme, achieved by matching computed results with expected results, obtained through a forward bio-optical model.

GAs are search methods inspired by evolutionary biology. The parameter set of the optimization problem is coded into a string, which plays the role of a chromosome, while single parameters represent genes. GAs work with a population of chromosomes (or individuals) and, following the rules of evolutionary biology, they are able to evolve the initial population by exploiting the mechanisms of cross-over and mutation. Then, the best individual (that is the best set of parameters) is selected according to the Darwinian principle of survival, that is expressed in terms of a fitness function, which measures the matching between computed and expected results.

Genetic programming has been used to estimate phytoplankton concentration in Case 1 and Case 2 waters on a simulated dataset of reflectances, achieving better results with respect to traditional polynomial fits and neural networks [31]. Also simultaneous retrieval of chlorophyll concentration, non-chlorophyllous particle and yellow substance absorption coefficients from sub-surface reflectance values has been tackled by means of a GA [32].

However, attention should be paid to the fact that, while gaining in accuracy, the complexity of the algorithm increases.

Chapter Three: Computational intelligence techniques

This chapter describes those computational intelligence techniques that have been used in this thesis, for the proposed applications to oil spill detection and bathymetry estimation from optical satellite images. In the previous chapter different approaches have been described for the study of ocean colour, and for the retrieval of sea water properties. We have seen that computational intelligence techniques have mainly been used in combination with a forward model in inverse problems, and that the necessary datasets for supervised learning and for testing are usually composed of simulated data, thus relying on direct models. The approach followed in this thesis consists in using computational intelligence techniques for remote sensing applications where it is possible to collect some measured data. This allows to study performance and generalization capabilities, in order to develop operational tools, whose aim is to exploit the power of optical satellite data for accessing and monitoring large marine areas. Thus, while this approach is affected by issues related to dataset construction, and attention must be paid when collecting data, it is not affected by model uncertainties, hypothesis and systematic errors. Unlike model-based approaches, or even hybrid approaches involving computational intelligence and analytic models, the approach chosen here is purely experimental, since it allows to derive models from data, without making any assumptions.

3.1 Neural networks

Artificial neural networks arose from the study of human brain, in the framework of neurosciences. They have been introduced in many fields of scientific research, with the aim of reproducing some of the typical activities of human brain, such as pattern recognition, or language interpretation. Thus, artificial neural networks have been developed in a way that resembles the structure of neural networks in the nervous system.

As a whole, human brain constitutes a complex nonlinear, parallel and massive information processing system, composed of a network of simple processing units, the neurons, which, acting together and, at the same time, influencing and being affected by other neurons, are able to accomplish difficult tasks.

In order to create an artificial neural network, able to mimic the behaviour of human brain, it is necessary to build a parallel and distributed structure, able to learn from previous experience, and to generalize (that is, to produce outputs in response to unknown inputs). This modelling starts from the basic processing units, artificial neurons. Learning is handled by connecting different neurons, and associating a weight to each connection (synapsis). These weights represent connection strengths, and their values are established during learning process. In the following sections two types of networks, which have been used in this thesis for oil spill classification, will be described.

3.1.1 Multi Layer Perceptron neural networks

A MLP neural network is a layered feedforward network model that maps sets of input data onto a set of outputs. In a layered feedforward network neurons are organized in layers, and signals propagate from the input layer to the output layer, thanks to the connections between each layer and the following [33].

Figure 6 shows a scheme of a MLP neural network architecture. The nodes (or neurons) of the input layer just propagate input values to the nodes of the first hidden layer. For each neuron belonging to a hidden layer the relationship between inputs and output (y) can be written as:

$$y = f\left(\sum_j w_j x_j + b\right) \tag{19}$$

where f is the *activation function*, that is usually a nonlinear function, x_j is the output from the j^{th} node of the previous layer, w_j is the weight of the connection between the j^{th} node of the previous layer and the current node, b is the *bias* of the current node, that is a threshold on the activation function.

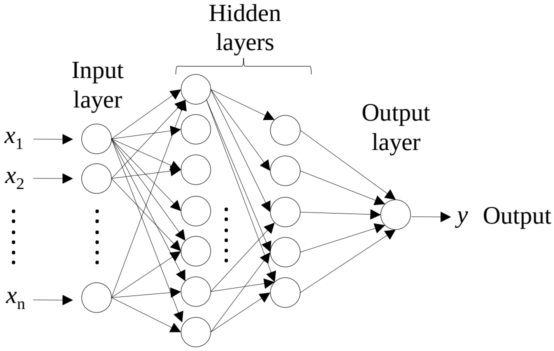

Figure 6:Scheme of a MLP neural network.

Typical activation functions are sigmoid functions, such as logistic function:

$$f(a) = \frac{1}{1 + \exp(-a)} \tag{20}$$

For the output layer, linear activation functions are often used. So doing, the network's output is a linear combination of nonlinear functions.

Learning occurs in the network by changing connection weights after each piece of data is processed, basing on the amount of error in the output, compared to the expected result. In the *backpropagation algorithm* the overall error of the network is computed starting from the output error, and propagating errors back through the network. This solution arises from the fact that desired values for the hidden neurons are not known.

3.1.2 Radial Basis Function neural networks

A RBF neural network is a layered network which is structured as in Figure 7. The input layer propagates inputs x_i, i=1...n, to the only hidden layer in the structure. Then, each node in the hidden layer performs a nonlinear transformation on its inputs, by means of the activation function, φ_j (*radial basis function*). Finally, outputs from each hidden neuron are weighted by the coefficients w_j, j=1...m (where m is the number of neurons in the hidden layer) and added in the single-node output layer to build the output y. Thus, the network's output can be written as a function of the input vector $\mathbf{x}=[x_1, ..., x_n]^T$:

$$y(\mathbf{x}) = w_0 + \sum_{j=1}^{m} w_j \varphi_j(\mathbf{x}) \tag{21}$$

where w_0 is a bias term. In a RBF network activation functions have a radial symmetry, whose shape is not decisive, provided that radial symmetry holds. Gaussian functions are usually employed:

$$\varphi_j(\mathbf{x}) = \exp\left(-\frac{\left\| \mathbf{x} - c_j \right\|^2}{r_j^{\,2}} \right) \tag{22}$$

where c_j is the centre, r_j is the spread (or radius), and $\| \; \|$ represents Euclidean norm.

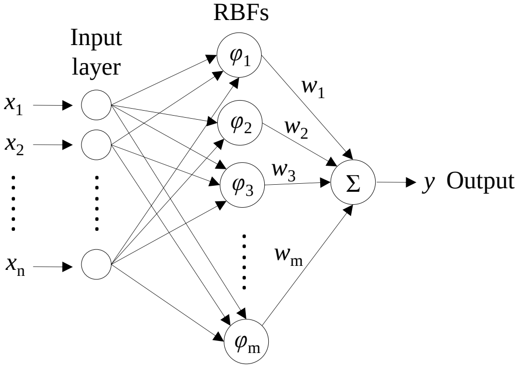

Figure 7: Scheme of a RBF neural network.

The network is trained by searching optimal values for centres, spreads and weights, according to the minimum error. The three sets of optimal parameters can be simultaneously retrieved with the *gradient descent algorithm*. Another approach consists in finding centres by means of a clustering algorithm, then, setting spreads by normalization, according to a maximum allowed distance between centres, and finally computing weights by means of the *least mean square algorithm*. A third approach consists in choosing random centres, setting spreads by normalization, and finding weights by means of the *pseudo-inverse method*.

3.2 ANFIS

This paragraph describes an example of a neuro-fuzzy technique that has been employed in this thesis, both for oil spill classification (Section 4.9) and for bathymetry estimation (Section 5.4). Neuro-fuzzy techniques are powerful tools, since they combine efficient learning algorithms, proper of neural networks, with the interpretability of fuzzy systems, resulting in a sort of grey-box modelling, that is a modelling strategy which describes the problem starting from the data, but that, unlike black-box models, is comprehensible and accessible.

Among the existing different types of neuro-fuzzy systems, here an Adaptive-Network-based Fuzzy Inference System (ANFIS) [34], is described. An adaptive network is a feed-forward neural network, where each node performs a specific function, and no weights are associated to the links between different nodes. The parameters involved in the node functions are updated in a supervised learning procedure, based on the gradient descent method. However, nodes can have parameters (adaptive nodes) or not (fixed nodes). ANFIS is an adaptive network which is functionally equivalent to a fuzzy inference system. Such networks are always composed of five layers, each having a specific function. For instance, in Figure 8 we consider a Takagi-Sugeno fuzzy inference system [35] and the equivalent ANFIS. The first layer performs the fuzzification of the inputs and is composed of adaptive nodes, whose parameters are the premise parameters: each input variable is connected to a number of nodes equal to the number of fuzzy sets used to model the variable, and each node corresponds to a membership function. Thus, the outputs of the first layer are the membership degrees. The second and the third layers are both composed of fixed nodes, each one corresponding to a single rule in the fuzzy inference system. The output of each node belonging to the second layer represents the firing strength of a rule, while the output of each node belonging to the third layer is the normalized firing strength, that is the firing strength divided by the sum of all firing strengths. The fourth layer performs the inference step. It is composed of adaptive nodes, whose parameters are the consequent parameters. Each node computes the consequent part of a rule, multiplied by its normalized firing strength. The last layer, composed of a single fixed node, performs the defuzzification step, computing the sum of the outputs of the fourth layer nodes. Thus, the overall output is obtained.

The supervised learning procedure for ANFIS can overcome some typical problems of the gradient descent method, such as slowness and tendency to be trapped into local minima. This is achieved by using a hybrid learning rule [36] [34], which combines the gradient descent backpropagation method for membership function parameters determination, with a Least Square Estimate (LSE) of the consequent parameters. This learning procedure divides each training epoch in two steps: a forward and a backward step. In the forward step, given some initial premise parameters, the network is fed with the input data, which go through the nodes until the output of the fourth layer is calculated. Then, consequent parameters are determined by means of the LSE and, once these parameters have been identified, the signal is passed to the fifth layer, and the overall error is computed. In the backward step, the error rates are propagated backward, and the membership function parameters, which are the premise parameters, are updated by means of the gradient descent method.

$$r_1 : IF\ X_1\ is\ A_{1,1}\ and\ X_2\ is\ A_{2,1}\ THEN\ y_1 = p_{1,0} + p_{1,1}X_1 + p_{1,2}X_2$$

$$r_2 : IF\ X_1\ is\ A_{1,2}\ and\ X_2\ is\ A_{2,2}\ THEN\ y_2 = p_{2,0} + p_{2,1}X_1 + p_{2,2}X_2$$

(a)

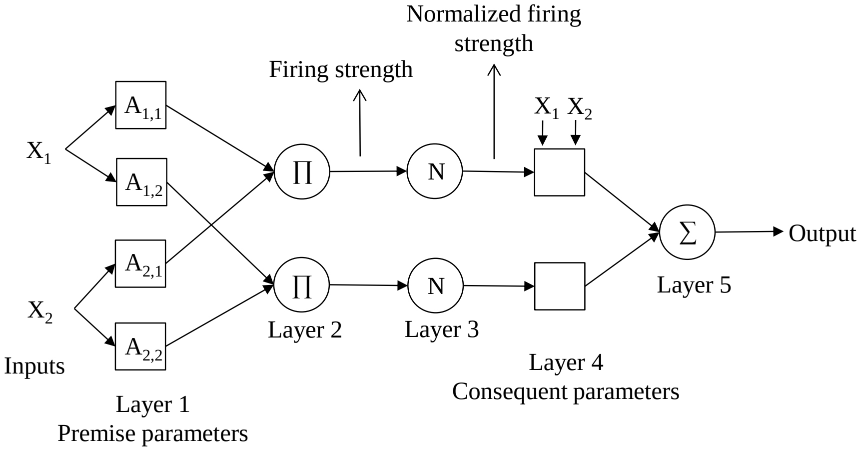

(b)

Figure 8: (a) Example of Takagi-Sugeno rules. (b) Equivalent ANFIS

3.3 Support Vector Machines

Support Vector Machines (SVMs), first introduced by Vapnik in the early eighties [37], represent a powerful technique for nonlinear classification and regression problems. We consider the problem of classifying a set of input vectors, defined in a F-dimensional space, into two classes. The problem can be represented as follows [38]: training data set is composed of pairs $\{\mathbf{x}_i, y_i\}$, where the input vector is $\mathbf{x}_i \in \Re^F$, and the output is $y_i \in \{-1,1\}$, where $y_i=1$ identifies positive elements and $y_i= -1$ identifies negatives. In the simple case of separable data, depicted in Figure 9, we suppose that in the F-dimensional space an hyperplane exists that separates positives from negatives. The hyperplane is identified by points $\mathbf{x}$ that satisfy the relation: $\mathbf{x} \cdot \mathbf{w} + b = 0$, where $\mathbf{w}$ is normal to the hyperplane and $b/\|\mathbf{w}\|$ is the distance from the origin. The *margin* is defined as the distance between the two positive and negative examples that are closest to the separating hyperplane. The support vector algorithm looks for the separating hyperplane with the largest margin. In mathematical terms, the margin is maximized when $\|\mathbf{w}\|^2$ is minimized, subject, for all elements, to constraints:

$$\mathbf{x}_i \cdot \mathbf{w} + b \geq +1 \quad \text{for} \quad y_i = +1 \tag{23a}$$

$$\mathbf{x}_i \cdot \mathbf{w} + b \leq -1 \quad \text{for} \quad y_i = -1 \tag{23b}$$

that can be written as a single inequality:

$$y_i (\mathbf{x}_i \cdot \mathbf{w} + b) - 1 \geq 0 \qquad \forall i \tag{24}$$

The problem can be solved using a Lagrangian formulation.

Nonlinear problems are solved by using nonlinear kernel functions that map data into a Hilbert space where the problem is linear.

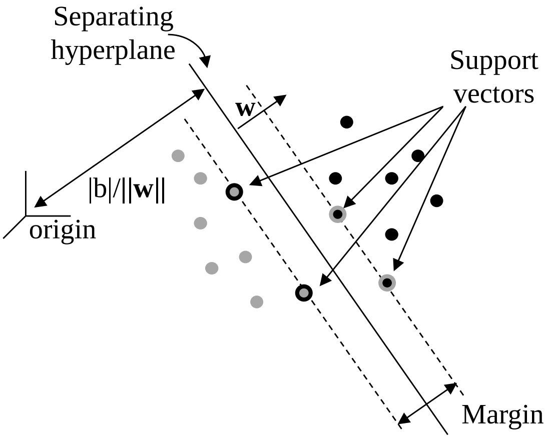

Figure 9: Linear separable case.

3.3.1 Cost-oriented -SVMs formulation

In case of non-separable data, the objective function of the previously described problem will grow arbitrarily large, thus some modifications are needed to the formulation. In order to deal with this problem, in 1995 Cortes and Vapnik proposed the cost-oriented (CO) formulation of SVMs [39]. The CO-SVM classification problem consists in maximizing the margin, though tolerating some errors, that is, allowing some positive class elements to be on the negative side, and some negative class elements to be on the positive side (see Figure 10). This is achieved by relaxing constraints in (23a), (23b), that become:

$$\mathbf{x}_i \cdot \mathbf{w} + b \geq +1 - \xi_i \quad \text{for} \quad y_i = +1, \quad \xi_i \geq 0, \forall\, i \tag{25a}$$

$$\mathbf{x}_i \cdot \mathbf{w} + b \leq -1 + \xi_i \quad \text{for} \quad y_i = -1, \quad \xi_i \geq 0, \forall\, i. \tag{25b}$$

Thus, for an error to occur, the corresponding ξ_i must exceed unity, so $\Sigma_i \xi_i$ is an upper bound on overall training error. The upper bound on the maximum distance between an element and the correct hyperplane determines the cost associated with the misclassification of that pattern. Thus, in order to account for the cost of all errors, a new term, which depends on $\Sigma_i \xi_i$, is added to the objective function to be minimized. This modification of the original (non cost-oriented) SVM classification makes the optimization process search for a tradeoff between a large margin and a small misclassification error penalty.

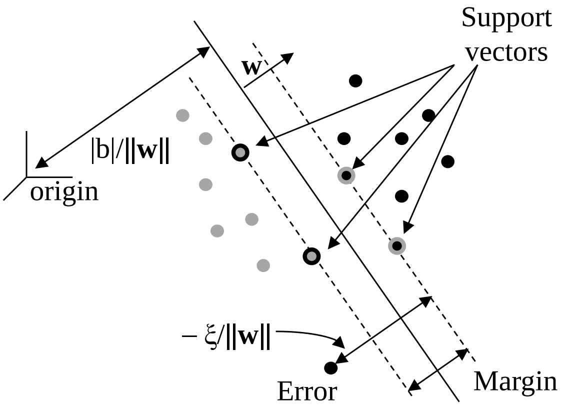

Figure 10: Non separable case. Cost-oriented formulation.

3.3.2 Incremental/Decremental SVMs formulation

The ID-SVM version that is considered in this thesis is the one presented by Cauwenberghs and Poggio in [40]. Their formulation of the incremental learning algorithm builds the solution recursively by adding one new point (pattern) at a time. The constraints for the SVM problem are retained on the previously considered patterns, while the new point is added adiabatically to the solution. At the same time, the decremental unlearning algorithm, in an analogous way, allows to remove data from the full trained solution, providing an efficient method to exactly evaluate leave-one-out generalization performance.

Such a classifier is able to update the solution adapting the classification to time varying conditions, making this approach more desirable than a batch one for applications where target conditions can change over time. Moreover, benefits are also obtained in terms of computational complexity.

Chapter Four: Application to oil spill detection from optical satellite images

4.1 Motivations

Today ninety per cent of oil and refined products are transported by the sea. In particular, out of the 1.5 to 1.8 billion tonnes of crude oil transported worldwide yearly, Europe is the main recipient, with nearly 500 million tonnes of crude oil and 250 to 300 million tonnes of refined products per year [41]. Moreover, many oil tankers transport their cargo to other destinations through European waters, meaning that the total amount of crude oil passing through European waters could be over 1 billion tonnes. Accidents resulting in massive and devastating oil spills, spread around by the mass media, affect public opinion and mobilise policy-makers. However, such dramatic accidents occur only occasionally and represent a small fraction of the pollution events at sea. Oil released into European seas as a result of operational discharges greatly exceeds the amount released during accidental spills. As an example, yearly, in the Mediterranean, these operations can add up to nearly 20 times the amount that was spilled by the "Prestige" off northern Spanish coasts in 2002 [42].

Due to the lack of adequate waste reception facilities in ports, added to poor surveillance, inadequate legislation systems, and the significant presence of companies and individuals without scruples, every year, at a lower cost, oil tanker crews release million of tonnes of oil from ballast waters and tank washing residues in our seas. More precisely, illegal dumping and routine operations of vessels account for between 666000 and over 2.5 million tonnes of hydrocarbons of marine pollution per year. It is estimated that at least 3000 major illegal hydrocarbon dumping incidents take place in European waters yearly. The Mediterranean is the sea that is most affected by this type of dumping, amounting to more than 400000 tonnes of released oil per year [41].

In this framework, the importance of developing efficient and cost effective monitoring tools can be easily understood. The exploitation of satellite images for oil spill detection allows to monitor large areas in an economical and easy way, thus offering many advantages in cost and time saving terms. The approach to oil spill detection which has been chosen in the present thesis consists in employing optical satellite data and using different intelligent classification systems. The motivations for the use of optical data will be explained in Section 4.4.

4.2 Oil spills in the marine environment

Whether originating from surface spillage or subsurface seepage, oil released at sea consists of a floating surface slick and suspended oil droplets within the water column. The chemical and physical properties of an oil are those who govern its optical characteristics and hence its appearance in remote sensing images. These features are also affected by weathering, which begins as soon as any oil is spilt, first through evaporation, then through dispersion and emulsification.

There are many different types of remote sensors which are able to recognize the presence of an oil slick on the sea surface, each one relies on some physical properties of oils.

Depending on the sensor used, there will be one oil property (or more oil properties) playing a major role in producing a different behaviour in the remotely sensed signal, with respect to clean water signal. Section 4.2.1 gives an overview of the main physical properties of crude and refined oils. In particular, attention is focused on the optical properties, which allow to discriminate oil from water in the visible and near infrared (NIR) wavelength range. Section 4.2.3 describes the creation of a detectable oil-water contrast in the upwelling radiance. Then, Section 4.3 gives an overview of the oil spill detection methods from satellite sensors, first introducing oil spill detection by means of SAR sensors, which is a mature and extensively used technology, and then focusing on the use of optical data, which represents the choice done in the present thesis, explaining the advantages and the issues related to this approach.

4.2.1 Some properties of crude and refined oils

Crude oils are complex mixtures of various hydrocarbons (aromatic and aliphatic), resins and asphaltenes. Refined products contain only a sub-set of these compounds each. The relative proportion of the various constituents determines both physical properties and optical characteristics of any given oil.

4.2.1.1 Chemical composition

Crude oils can be classified according to the relative amount of n-alkanes, branched alkanes, cycloalkanes, aromatic hydrocarbons and NSO compounds:

- Paraffinic oils: mainly composed of acyclic alkanes, these oils have a low sulphur content.
- Paraffinic-naphthenic (or mixed-base) oils: composed of both cyclic and acyclic alkanes, these oils have a low sulphur content. The majority of crude oils belongs to this group.
- Aromatic-intermediate oils: these oils contain more than 50% aromatic hydrocarbons and usually have a higher content of NSO-compounds, particularly those containing sulphur.

Refined oils are distillation products of crude oils, and are classified according to the number of carbon-atoms contained in the molecules making up the mixture. In decreasing order of volatility (increasing density and viscosity) these are:

- Petrol and naphtha with benzene and other volatile oils (C4-C10).
- Kerosene and lamp oils (C11-C13).
- Diesel and light gas oils (C14-C18).
- Heavy gas oils, home heating oils (C19-C25).
- Lubricating oils, light fuel oils (C26-C40).
- Residual and heavy fuel oils (>C40).

4.2.1.2 Density and specific gravity

Oil density is often measured relative to water, in order to obtain a dimensionless quantity, specific gravity (SG). Most oils are lighter than water, and, in particular, crude oils are often divided into light, medium and heavy, on the basis of American Petroleum Institute (API) gravity measurements [43]:

$$°API = \left(\frac{141.5}{SG_{60F}} \right) - 131.5 \qquad (26)$$

where SG_{60} is the specific gravity of the oil at 60°F, (i.e. the ratio between oil density at 60°F and pure water density at the same temperature). The API scale is thus inversely proportional to density. Basing on API definition, the following classes have been specified:

- Light crudes: API gravity ≥ 30°API ($SG \leq 0.87$).
- Medium crudes: API gravity between 22°API and 30°API ($0.87 < SG \leq 0.92$).
- Heavy crudes: API gravity between 10°API and 22°API ($0.92 < SG \leq 1.00$).
- Tars or tar-sands: API gravity < 10°API, ($SG \geq 1.00$).

4.2.1.3 Viscosity

The viscosity of an oil is a measure of the oil's resistance to shear, so it is a measure of its resistance to flow. When viscosity is determined by directly measuring shear stress and shear rate, it is expressed in centipoise (cP) or in Pa s (1 cP =1 mPa s), and is referred to as the absolute or dynamic viscosity. For instance, water at 20°C has a dynamic viscosity of 1 cP. The viscosity of single-compound hydrocarbons increases with the number of carbon atoms contained in a molecule. High molecular weight hydrocarbons are generally soluble in low-molecular weight alkanes or aromatics, and the viscosity of the mixture depends on the relative content of low and high-molecular weight compounds. Viscosity also varies with density. Light oils have viscosities less than 30mPa s at 20°C, while heavy asphaltic oils have viscosities measured in thousands of mPa s. For natural tars viscosity is usually greater than 10^4 mPa s [44].

4.2.2 Oil optical properties

Inherent optical properties that are relevant for oil detection are: absorption, fluorescence and refractive index. Scattering is a small effect at visible wavelengths and it usually has a magnitude and spectral behaviour close to that of pure sea water.

4.2.2.1 Absorption

Typical crude oil spectra show strong absorption at short wavelengths, that range from ultraviolet (UV) or violet for the lightest oils, to red or NIR for the heaviest crudes. Absorption coefficients decrease exponentially towards longer wavelengths. Decay widths do not vary much within crude oils. Actually, this behaviour is similar to that of CDOM, so that it may be difficult to distinguish the spectral signature of dispersed oil from that of CDOM. Refined oils have an anomalous behaviour, due to the process of fractionation. In particular, the absorption coefficient of light refined oils decreases steeply towards visible wavelengths, while heavy refined oils show lower absorption in the UV, but larger decay widths extending to NIR wavelengths.

4.2.2.2 Fluorescence

Oil fluorescence is generally excited by light at UV to blue wavelengths. The spectral fluorescence properties of oils when excited by laser pulses can be used to distinguish between different oil types. Generally speaking, as excitation wavelength increases fluorescence is induced in a smaller number of compounds, thus, light oils fluoresce at shorter wavelengths, from UV to green, while heavy oils show broader fluorescence spectra which peak at longer wavelengths [45]. Solar radiance could also induce oil fluorescence, but, since it is less intense than excitation by laser, the fluorescence signal will be weaker. However, solar induced fluorescence may contribute to solar reflectance on particularly bright days. Fluorescence peaks vary in width and wavelength position according to oil type, and decay exponentially toward the red and NIR.

4.2.2.3 Refraction

Oil refractive index is greater than that of sea water (≈1.34) at visible and NIR wavelengths. There is a significant variability between oil types, but usually heavy oils have a higher refractive index. For crude oils the refractive index lies between 1.57 and 1.67 in the UV and between 1.48 and 1.52 in the visible [46]. Refractive index of course influence light specular reflection at the air-sea interface for clean and oil covered sea surfaces.

4.2.3 Oil-water contrast

The presence of an oil film on the sea surface implies some modifications in the upwelling radiance, and thus in the remote sensing reflectance (11) measured over the sea surface.
In particular, the optical properties of crude and refined oils allow to distinguish them from water. More precisely, as we have mentioned before:

- Oil refractive index is greater than that of sea water.
- Oil absorption coefficients are several orders of magnitude greater than that of water in the blue, and decay exponentially with wavelength.
- Crude and refined oils fluoresce when subjected to bright natural light, with fluorescence peaks that vary in width and wavelength position according to oil type, and decay exponentially towards the red and NIR.

These characteristics contribute to the detectable oil water contrast. This can be described by analysing the contributions to upwelling radiance measured above an oil film [47], which are represented in Figure 11.

- Atmospheric path radiance (a): this contribution should be removed, but for oil spill monitoring applications this is not essential.
- Specular reflection of sky radiance (b): this contribution is greater from an oil covered sea water surface due to oil’s higher refractive index. Contributions due to reflection at the oil-water interface are two orders of magnitude lower than at the air-oil interface, and may thus be neglected.

- Water-leaving radiance (c): this contribution arises from a portion of incident light that is transmitted through the surface, and scattered back up by the sea water and its constituents. The presence of an oil film has a double effect on this contribution: reduced transmittance through the air-oil interface and absorption within the oil layer. When the oil is sufficiently thick, all light is absorbed and further increases in oil thickness are not detectable. This limiting thickness depends on the oil absorption coefficient and the wavelength of the light, from 0.02mm for heavy crudes at 440nm to about 2mm for light crudes at 750nm [48].
- Oil fluorescence and scattering (d): oil fluorescence excited by sun light in the UV and scattering from water entrained in the oil also contribute. In particular, in heavier oils with high absorption coefficients throughout the optical range, this contribution is low. The absorption coefficient of light crudes decays more rapidly, so fluorescence and scattering may give a significant contribution at longer wavelengths.

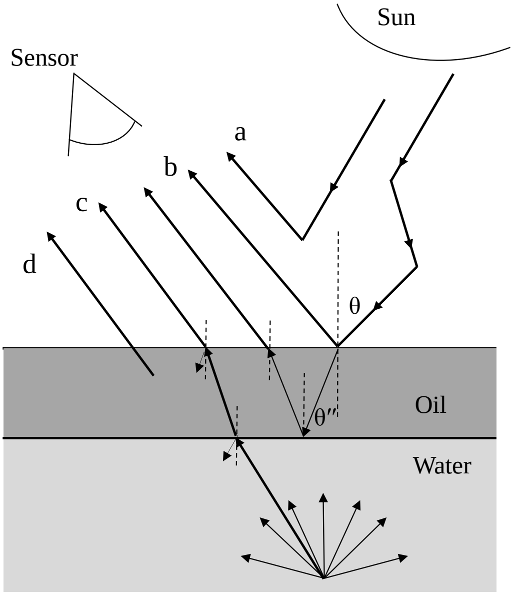

Figure 11: Contributions to radiance measured above an oil covered sea water surface. (a) Atmospheric path radiance. (b) Specular reflection of sky radiance. (c) Water leaving radiance. (d) Fluorescence and scattering contributions.

Oil-water contrast, *C*, can be defined as the difference between the remote sensing reflectance, defined in (11), in presence of an oil film, and remote sensing reflectance of clean water, normalized to remote sensing reflectance of clean water (in the following angular and wavelength dependence are omitted for simplicity):

$$C = \frac{R_{rs}^{(oil)} - R_{rs}^{(clean\,water)}}{R_{rs}^{(clean\,water)}}. \tag{27}$$

Taking into account all the above mentioned contributions, the contrast can be written as [47]:

$$C = \frac{\left(r_o - r_w\right)R_{rs}^{(sky)} - \left(t_w t_{dw} - t_o t_{do} e^{-\left[1/\mu_d + 1/\cos\theta''\right]a_0 z}\right)R_{rs} + F_o + B_o}{r_w R_{rs}^{(sky)} - t_w t_{dw} R_{rs} + P} \tag{28}$$

where $R_{rs}^{(sky)}$ represents the sky remote sensing reflectance (that is remote sensing reflectance, defined in (11), where the numerator is only sky radiance), r_o and r_w are the specular reflection (Fresnel) coefficients for oil and water, R_{rs} is the remote sensing reflectance, t_o and t_w are the Fresnel transmittance coefficients for oil and water, t_{do} and t_{dw} are the diffuse transmittance coefficients for incident light, a_o is the oil absorption coefficient, z is oil thickness, μ_d is the average cosine of downwelling irradiance defined in (9a) within the oil, F represents oil fluorescence, B represents scattering by water in the oil, and P the atmospheric contribution. It is clear from (28) that oil-water contrast depends on many factors, that are oil type, oil thickness, water constituents, which affect scattering and absorption in the sea water and atmosphere contribution. Thus, contrast can be positive or negative depending on water type and on environmental conditions, but it also vary according to wavelength, since absorption and fluorescence have a strong spectral dependence. Thus, for a given oil on a sea water surface, C can be positive in some spectral regions and negative in others. In particular, from (28) we can observe that C is positive when:

$$\left(r_o - r_w\right)R_{rs}^{(sky)} + F_o + B_o > \left(t_w t_{dw} - t_o t_{do} e^{-\left[1/\mu_d + 1/\cos\theta''\right]a_0 z}\right)R_{rs}\,. \tag{29}$$

For thin oils this occurs at wavelengths where $R_{rs}^{(sky)}$ is high, or where R_{rs} is low, usually the violet and blue (between 400nm and 480nm), and NIR (starting at 700nm). As thickness increases the exponential term approaches 0, and contrast becomes negative throughout most of the visible spectrum. In the NIR R_{rs} is negligible, due to high water absorption, and the contrast is positive, except when there is a high concentration of scattering particles in water. However, near the sea water reflectance peak, between 480 and 570nm in coastal waters, R_{rs} may be sufficiently high to give low or negative contrast even for thin oils.

The change in contrast between oil spills and sea water, depending on both oil type and water type, for different sun-observer geometries, as also been investigated in [49] [50].

4.3 Overview of oil spill detection methods using satellite sensors

Many different remote sensing instruments are able to detect oil spills at sea [51], some of them are already in use for operational services. Among these, the most widely used are radar based systems, such as SAR instruments, because of their all-weather and all-day capabilities. Side-Looking Airborne Radar (SLAR) is an alternative to SAR: it is an older but less expensive technology than SAR, but SAR has greater range and resolution [52]. Moreover, airborne surveillance is limited by the high costs and is less efficient for wide area surveillance, due to its low coverage. Radar based instruments are able to detect oil spills thanks to the difference between oil and water in wave-dumping capacity. A radar image of the sea surface is formed by reconstructing the reflection of active radar signals from small gravity and capillary waves. The presence of an oil slick, due to oil's viscosity, suppresses capillary ripples, so that the return signal from an oil covered surface is smaller. Thus, oil slicks appear as dark objects in SAR images. However, calm sea regions appear as dark objects too, and represent a source of error for oil spill detection. Sea state is a limiting factor for SAR oil spill detection. In particular, for wind speeds below 1.5 m/s the wind-stress is insufficient to generate ripples, while above 12 m/s the oil film is disrupted and washed down by breaking waves [53]. More precisely, the optimal wind velocity range for oil spill detection has been estimated to be between 1.5 m/s and 6 m/s [54].

Microwave (MW) radiometers are passive sensors which measure the microwave radiation emitted in the wavelength range from mm to cm, and are all-weather and all-day operability instruments. Since oil slicks emit stronger microwave radiation than the water, they appear as bright objects on a darker sea in MW radiometer images. As reported in [51], according to [55], these instruments could potentially be used for measuring slick thickness, but the required resolution is such that aircraft platforms are more appropriate than satellite ones.

Thermal infrared (IR) imagers are passive sensors operating in the wavelength range between 8 μm and 13 μm. In this region oil has a lower emissivity than sea water, thus, oil slicks of medium thickness appear as cool objects in IR images, leading to negative contrast [48]. There is a threshold thickness at which contrast is sufficient for oil detection: usually it is not possible to detect oils having thickness below 50 μm. Regarding thick oil slicks, during the day these slicks absorb solar radiation, and become warmer than the surrounding sea, giving increasingly positive oil-water contrast in thermal images as thickness increases. At a given thickness, which is usually about 250 μm, the increase in emission arising from higher oil temperature will balance the negative oil-water contrast arising from the lower emissivity of the oil. Above this threshold, oil appears brighter in images acquired at night, below it, darker. The threshold thickness depends on environmental conditions and on the absorption and emissivity properties of the oil. However, the oil spills may not have a significant different temperature signature from the surrounding water at night [51].

UV imagers are passive sensors which can be used to detect oil spills, since an oil layer is a good reflector of UV radiation. Although the contrast with sea water is low, even layers as thin as 0.01μm may reflect the UV component of incident sunlight towards the sensor. Solar induced fluorescence also contributes to the signal. UV instruments are not usable at night, and wind slicks, sun glints and biogenic material can cause false alarms in the UV data.

As UV imagers, visible (VIS) and NIR spectroradiometers provide images of daylight-reflected solar radiation, and rely on differences in oil and water optical properties in order to detect the presence of an oil slick. These instruments necessitate of day light and are affected by the presence of clouds. However, the availability of multiple wavelengths can give additional information to distinguish, for instance, slicks produced by algal blooms from oil spills. Moreover, the use of this instruments is not limited by sea state conditions and could be a useful support to SAR-based systems, since calm sea regions do not bring any false alarm in optical images. As Section 4.4 will discuss, optical data show a great potential as a tool for improving oil spill detection from satellite instruments, so it is worth exploring the possibility of an optical investigation, which is object of the first application proposed in this thesis.

4.3.1 Oil spill detection using SAR satellite images

As stated before, since SAR data have been widely exploited for oil spill detection, many contributions can be found in the literature regarding the study of oil slicks in SAR images, and several efforts have been made in order to develop automatic detection systems. Images from remote sensing instruments, in particular SAR images, are usually combined with information from trained and experienced human observers. Visual observation relies on many of the same physical mechanisms which are used by various remote sensing instruments, and which give rise to the perception of colour (wavelength distribution), brightness (signal intensity) differences between oil and water, variations in surface roughness (wave damping), and finally the interpretation of spatial patterns, and the analysis of surrounding elements (e.g. proximity to land, presence of other similar objects in the scene etc...). Thus, a fully automated or semi-automated system for oil spill detection should actually resemble the expert's decisions based on similar criteria, knowledge and rules, and this has been subject of several studies reported in literature.

In 2008 Kubat *et al.* [56] proposed a neural network for the classification of dark regions detected in SAR images, to be used as a training set of the system. In their paper the authors also analyse in detail the issues related to the application of machine learning techniques to oil spill detection. Del Frate *et al.* [57] also used a neural network architecture for semi-automatic detection of oil spills in SAR images, building an input vector for the network, containing a set of features which characterize oil spill candidates. Later, Topouzelis *et al.* [58] compared the performance obtained using MLP and RBF neural networks. In particular, the authors used original reconstructed SAR images as input for the classification system, instead of using a vector of features extracted from dark regions in the images. Solberg *et al.* [59] developed a semi-automated classifier for oil spill detection, based on statistical modelling combined with a rule-base approach. They identified eleven different object characteristics [60] and used them to build a classification procedure based on Bayesian inference, where three different categories of real oil spill probability (low, medium and high) were recognized. Fiscella *et al.* [61] developed a stochastic classifier based on Mahalanobis statistical tests and classical compound probabilities.

Fuzzy logic systems, able to better resemble a human expert's decision, have also been used by Keramitsoglu *et al.* [62] to develop a fully automated system for oil spill identification in SAR images.

4.4 Oil spill detection using optical satellite images

We have seen that SAR images have been widely used for oil spill detection, as they are not affected by local weather conditions and cloudiness. Currently, many government institutions already use SAR technology-based services for oil spill detection, but the high false alarm rate makes these systems not enough reliable, so that many detected spills are followed by no action, due to the risk of expensive in situ missions which could turn out to be false alarms. Thus, there is a need for more reliable systems. This suggests the possibility of exploiting optical data, which, up to now, have been little used for oil spill detection applications. The development of a new approach, based on optical data, could be used either on its own or as a support to SAR-based solutions, in order to meet the need of environmental protection authorities for efficient and cost effective monitoring tools, also considering that optical satellite images are cheaper (sometimes freely available), and provide more frequent (daily) information if compared to SAR images, allowing for large areas monitoring and remote zones control.

The reason why optical satellite images have been little used in the field of operational oil spill detection, is that good weather conditions and day light are mandatory conditions to perform a correct detection, while this conditions are not required when using SAR data. However, the use of SAR data implies many other limiting factors, such as cost, low revisit time, and sea state, since the optimal wind velocity range for oil spill detection is between 1.5 m/s and 6 m/s [54].

The use of optical data can improve operational monitoring for many reasons. The key point is that oil spill identification by optical sensors and by SAR sensors rely on different mechanisms, that are respectively controlled by differences in oil and water optical properties, which give rise to oil-water contrast, as explained in Section 4.2.3, and by differences in oil and water wave-damping capacity. Thus, oil spill detection systems based on optical data are not affected by the same false alarm types (such as very calm sea areas) as SAR-based systems. Moreover, while MW, IR and UV radiation are strongly absorbed by water, visible radiation can penetrate water to a depth of many meters, especially in the blue. Hence, optical sensors operating in the visible range of the spectrum can potentially detect oil not only on the surface, but also dispersed in the water column.

The possibility of detecting oil spills from optical data has also been demonstrated in [63], where the authors use optical images, captured by NASA’s Moderate Resolution Imaging Spectroradiometer (MODIS, see Table 1), to access the magnitude, area covered and duration of a big oil spill occurred in Lake Maracaibo, Venezuela, caused by several accidents happened to the oil industry operating in the lake’s area. More recently, empirical relationships based on MODIS higher resolution bands (250 m) have been used to detect oil spills in the Arabian Sea [64]. MODIS images have also been used to detect natural crude oil slicks and consequently estimate the annual seepage rates in the northwestern Gulf of Mexico [65]. These studies prove that oil spill identification from optical images, in particular those acquired by MODIS, is possible, and it can be used for operational monitoring. Beside this, the interpretation of the remotely sensed multi-spectral signal produced by an oil slick on the sea surface appears to be quite problematic, because, as explained in Section 4.2.3, many factors contribute to oil-water contrast, such as oil type, oil absorption properties, oil thickness, and water constituent concentrations. These factors often give conflicting contributions, which vary through the visible and NIR spectral range. An additional issue is represented by the difficulty in performing an accurate atmospheric correction, in order to reduce path radiance contribution, and by the presence of sunglint. These factors make spectral analysis a difficult task.

The approach to oil spill detection which has been chosen in the present thesis consists in employing optical data from MODIS sensor and using different intelligent classification systems, which avoid any spectral analysis. The identification of oil spills is then mainly based on geometrical features, together with differences in the contrast. The use of supervised computational intelligence techniques allows to overcome difficulties related to contrast interpretation and atmospheric correction, which are typical of an analytic approach.

4.5 A software architecture for optical oil spill detection

In this chapter the attention is focused on different classification techniques, suitable for discriminating between true oil spills and other phenomena in multi-spectral satellite images of a marine scenario. In order to do this, it is necessary to identify oil spill candidates in the image, to extract some features which allow to characterize oil spills, and to feed the classifier with these features. However, an automated system for oil spill classification will accomplish other pre-processing tasks. Figure 12 shows a software architecture for image processing and automatic classification of oil spill candidates in multi-spectral images.

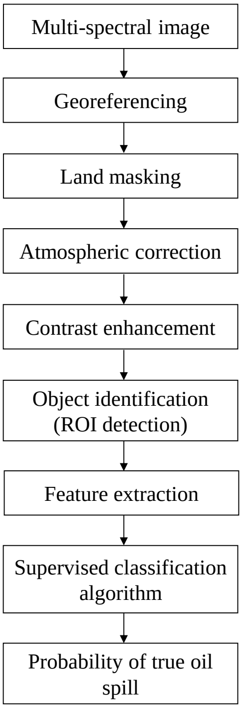

Figure 12: Scheme of the proposed oil spill detection system.

The input of the system is a multi-spectral image. In this thesis MODIS images at level L1B have been used, but images from other sensors (provided that they have equivalent bands) could be used as well. In the pre-processing phase the image is georeferenced, a land mask is applied and atmospheric effects are softened through the atmospheric correction module. In this latter phase, ancillary information regarding atmospheric conditions, such as ozone and water vapour concentrations, are necessary, and must be retrieved from other sensors or data. However, this is an optional step. A local histogram equalization for contrast enhancement allows to emphasize the presence of oil spill candidates in the image. Then, regions of interest are identified by a clustering algorithm (*k*-means, FCM, …). For each selected region the feature extraction module computes a set of features which serves as input for the supervised classification procedure, in order to discriminate between oil spills and other phenomena. The output of the system is the probability of the selected object to be an oil spill.

4.6 The dataset

The supervised learning procedure necessitates of a dataset of input and target elements which serves partly for training the classifier and partly for testing the classification performance. As anticipated in Section 2.2, dataset collection represents a relevant issue for computational intelligence technique applications. Training set size must be appropriate to the number of unknown parameters in the classifier structure. In addition, elements in the dataset must compose a representative set of the data the trained classifier will process.

For the present study a considerable dataset of regions of interest has been built by collecting a number of optical images taken during the years 2008 and 2009, over the entire area of the Mediterranean Sea. In particular, level L1B data from MODIS sensor have been used, having a spatial resolution of 250 m. Level L1B data consist in calibrated radiance or reflectance values, which are freely available from NASA [66]. MODIS instrument is aboard Terra and Aqua satellites. Terra's orbit around the Earth is timed so that it passes from north to south across the equator in the morning, while Aqua passes south to north over the equator in the afternoon (see Table 3). Using data from both MODIS-Terra and MODIS-Aqua sensors, up to four images per day are available, each one partially covering the Mediterranean Sea.

As Table 4 shows, only bands 1 and 2, respectively centred in the VIS at 0.65 μm and in the NIR at 0.85 μm, are available from MODIS at the highest resolution, so that any spectral analysis is precluded. On the other hand, it is important to have a spatial resolution as good as possible, since most slicks produced by illegal discharge from moving ships could not be detected in lower resolution images (e.g. 1km) due to their small area.

Table 3: MODIS specifications.

Orbit	Altitude: 705 km, 10:30 a.m. descending node (Terra) or 1:30 p.m. ascending node (Aqua), sun-synchronous, near-polar, circular
Scan Rate	20.3 rpm, cross track
Swath Dimensions	2330 km (cross track) by 10 km (along track at nadir)
Quantization	12 bits

Table 4: MODIS bands and spatial resolution.

Primary Use	**Band**	**Bandwidth** (Bands 1-19 are in nm; Bands 20-36 are in µm)	**Spatial resolution** (m)
Land/Cloud/Aerosols Boundaries	1	620-670	250
	2	841-876	
Land/Cloud/Aerosols Properties	3	459-479	500
	4	545-565	
	5	1230-1250	
	6	1628-1652	
	7	2105-2155	
Ocean Colour/Phytoplankton/ Biogeochemistry	8	405-420	1000
	9	438-448	
	10	483-493	
	11	526-536	
	12	546-556	
	13	662-672	
	14	673-683	
	15	743-753	
	16	862-877	
Atmospheric Water Vapour	17	890-920	
	18	931-941	
	19	915-965	

Only images acquired in clear sky conditions have been selected when building the dataset. After georeferencing, a local contrast enhancement, based on histogram equalization, has been applied in order to improve the visualization. Then, possible oil slicks have been detected by visual inspection performed by a trained interpreter, basing on his previous experience, and corresponding regions of interest have been selected through a fully manual procedure. In order to increase the reliability of the regions of interest identified in MODIS data, for each selected image the corresponding Envisat-ASAR image, at 150 m spatial resolution, has been analysed for comparison. Unfortunately, due to sunglint and weather conditions, only approximately 10% of the MODIS images could be used for comparison. However, for many of the selected cases ground truth was available. More precisely, many cases correspond to oil slicks that have been verified by the Italian Coast Guard during specific operations for oil dispersion.

Selected regions have been divided into two classes: the first class is composed by regions identified by photointerpretation as possible oil spills, on the basis of the contrast between regions and surrounding areas (which are supposed to be clean waters). The second class is composed by regions identified as look-alikes, which could be for instance algal blooms or sea currents etc... The analysis has been conducted examining the scene where the candidate oil spill or look-alike had been detected, that is, considering the context, the location and the possible presence of other elements in the surrounding area. This allows to distinguish between linear slicks, which might be caused by a moving ship releasing oil, as shown in Figure 13 (a), and sea currents, usually occurring in particular spatial patterns, such as those shown in Figure 13 (b).

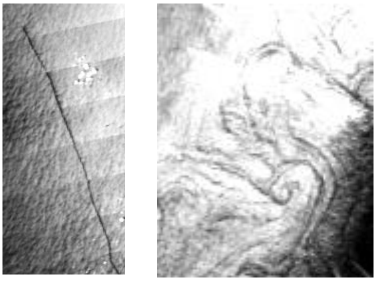

(a) *(b)*

Figure 13: (a) An oil spill case from the dataset. (b) A look-alike case from the dataset.

In the end, the number of detected oil slicks is approximately equal to the number of look-alikes, for a total of 316 elements. A search for multivariate outliers has also been performed basing on the distribution of some features (see Section 4.7) characterizing oil spills. After this analysis, 12 elements have been removed, obtaining a dataset composed of 304 elements, 157 oil spills and 147 look-alikes. The outliers resulted to be represented by big nonlinear shaped slicks and dark regions in a particularly complex background, which will not be considered in this application. The reason for this choice is motivated by the fact that the classification system proposed in this thesis is intended for identification of illegal oil discharge by moving ships, or of oil released during tank cleaning in the sea. Thus, since training elements should resemble data the classifier will be asked to process in the finished application, only these types of slicks have to be well represented in the dataset. Very big slicks, produced for instance by oil tanker accidents, which can cause environmental disasters to happen, have not been handled, since the appropriate authorities are usually informed about these events. In such cases, time series of satellite images can be used to estimate the quantity of spilled oil, the area affected by oil pollution and to follow its spatial and temporal evolution, while a classification system based on optical data for quick alert is unnecessary. On the other hand, the importance of focusing the attention on operational discharges and of developing efficient and economic monitoring tools has already been explained in Section 4.1.

4.7 Feature description

In order to discriminate between oil spills and look-alikes, a number of physical and geometrical features characterizing the object to be classified have been exploited. These features are computed by the feature extraction module (see scheme in Figure 12) and are used as input for the classification system.

Following the results of SAR oil spill detection [51] [59] [57], a set of gray level features, characterizing the differences between the object and the surrounding area, and a set of geometrical features, describing shape and extension, have been used:

1) Geometrical features

- *Area of the object* (A) expressed in km^2.
- *Perimeter* (P) expressed in km.
- *Complexity* (C): defined as

$$C = \frac{P}{2\sqrt{\pi A}}.$$

This feature generally assumes small numerical values for regions with simple geometry and larger values for regions with complex geometry.

- *Spreading* (S): computed performing a principal component analysis on the vector whose components are the coordinates of the pixels belonging to the object:

$$S = \frac{100\lambda_2}{\lambda_1 + \lambda_2},$$

where λ_1 and λ_2 are the two eigenvalues associated with the covariance matrix ($\lambda_1 > \lambda_2$). This feature assumes low values for long and thin objects and high values for objects closer to a circular shape.

2) Gray level features

- *Object Standard Deviation*: standard deviation of the intensity values of pixels belonging to the object.
- *Max Contrast*: difference between the background mean intensity value and the lowest intensity value inside the object.
- *Mean Contrast*: difference between the background mean intensity value and the object mean intensity value.

Spectral features have not been used, since the two bands available from MODIS full resolution images are insufficient for a spectral analysis. Gray level features have been calculated on a two-band ratio (band 2/band 1) so as not to consider the atmosphere contribution.

Table 5 and Table 6 report some statistical parameters of the above mentioned set of features, computed for the 157 oil spill and 147 look-alike cases in the dataset where outliers had been removed. The tables show that oil spills are generally smaller and have a thinner shape. This is consistent with the choice of considering slicks produced by moving ships.

Table 5: Statistical parameters of the features calculated for oil spill cases in the dataset.

Feature	Min	Max	Mean	Std. Dev.
Area (km^2)	0.688	41.7	6.96	6.58
Perimeter (km)	2.91	94.6	20.4	15.9
Complexity	0.229	5.40	2.16	0.770
Std. Dev. band ratio	0.00610	0.0519	0.0199	0.00940
Mean Contrast band ratio	-0.0588	0.156	0.0505	0.0311
Max Contrast band ratio	-0.0255	0.216	0.0933	0.0449
Spreading	0.114	26.8	4.25	5.35

Table 6: Statistical parameters of the features calculated for look-alike cases in the dataset.

Feature	Min	Max	Mean	Std. Dev.
Area (km^2)	0.875	73.9	14.4	14.7
Perimeter (km)	1.00	147	26.4	21.2
Complexity	0.0912	5.009	2.016	0.893
Std. Dev. band ratio	0.00521	0.0999	0.0283	0.0179
Mean Contrast band ratio	-0.00535	0.234	0.0733	0.0519
Max Contrast band ratio	0.0198	0.451	0.134	0.0822
Spreading	0.548	44.3	11.9	10.0

4.8 First batch classification approach: statistical classifiers and neural networks

As a first attempt to oil spill classification, a set of statistical classifiers and neural networks have been applied to the extracted features, adopting a batch approach, that is, considering the overall dataset. The classifiers have been trained using 60% randomly chosen examples of the available dataset, while the remaining 40% were used as a test set, in order to evaluate the classification performance of the different methods. In particular, normal density-based linear and quadratic classifiers have been employed, as well as a logistic regression-based linear classifier. A value of 0.5 has been used as *a priori* probability for both oil spill and look-alike classes. Concerning non linear classification, three *k*-nearest neighbour classifiers and two neural networks, namely a RBF and a MLP have been used. The MLP neural network has been trained by a backpropagation algorithm and different topologies have been used (1 hidden layer and different numbers of hidden neurons), using logistic activation functions for the hidden neurons and a linear activation function for the output layer. Different architectures have also been tested for the RBF network, where Gaussian basis functions have been used.

Table 7 shows the performance of the different classifiers in terms of mean percentage of correct classification, calculated on the training set and on the test set. The relative error is estimated by considering deviations from the mean value. Among the examined classifiers, the best performance on the test set is obtained by the MLP neural network with 1 hidden layer composed by 6 neurons.

Table 7: Classifier performances: the estimated relative error is 2%.

Classifier	Mean training set correct classification %	Mean test set correct classification %
Normal density based linear	79	74
Normal density based quadratic	77	75
Logistic regression	80	74
1-nearest neighbor	100	71
2-nearest neighbor	92	75
3-nearest neighbor	88	76
RBF (10 neurons)	76	65
MLP (6 hidden neurons)	92	**79**

As regards misclassified examples, false negatives (i.e. oil spills erroneously classified as look-alikes) are usually characterized by high spreading values or small area values, while false positives (i.e. look-alikes erroneously classified as oil spills) are represented by a more heterogeneous set.

Results obtained with the same batch classification approach, applied to a smaller and earlier version of the presented dataset are shown in [67].

4.9 Second batch classification approach: ANFIS

Following the idea that an automatic system for oil spill detection should resemble an expert's decision, as a second batch classification approach a more interpretable machine learning technique, ANFIS [34] (see Section 3.2), has been investigated. Regarding performance evaluation, we have to consider that in a two-class problem the use of classification accuracy can be inappropriate, because it assumes equal error costs for misclassification of target class elements. However, for many applications, such as oil spill classification, this condition is not satisfied. As stated before in the text, one of the main issues related to oil spill classification is the necessity of keeping false alarm rate as low as possible, because false alarms could bring environmental protection authorities to unnecessary (and expensive) actions. As a consequence, misclassification cost for the oil spill class results to be higher than misclassification cost for the look-alike class. Thus, it is important to adopt a performance measure that works even in presence of different costs between the two classes. In order to account for this, Receiver Operating Characteristic (ROC) analysis [68] has been exploited.

4.9.1 ROC analysis

ANFIS is a continuous classifier, $\Gamma(x)$, for a two-class problem, that is a mapping from the F-dimensional space (F is the number of features) to the interval [0,1]:

$$\Gamma(x)\colon \Re^F \rightarrow [0,1]. \tag{30}$$

To obtain a binary classifier, we must choose a threshold τ on the classifier output. More precisely, if we call the two classes positives and negatives[1] the binary classifier can be represented as follows:

$$\Gamma_\tau(x): \begin{cases} \mathrm{N} & \mathit{if}\ \Gamma(x) < \tau \\ \mathrm{Y} & \mathit{if}\ \Gamma(x) \geq \tau \end{cases} \tag{31}$$

where $0 \leq \tau \leq 1$, N and Y stand for negative and positive classifications, respectively. This resulting binary classifier, $\Gamma_\tau(x)$, can be coupled to a pair (TPR, FPR), where TPR and FPR are, respectively, the True Positive Rate (the ratio of positives correctly classified to total positives) and the False Positive Rate (the ratio of negatives incorrectly classified to total negatives)[2]. The continuous classifier can thus be associated with a set of pairs (TPR_{τ_i} , FPR_{τ_i}), i=1,…, I, where I is the number of thresholds τ. This allows to evaluate the performance of the continuous classifier in the space (TPR, FPR), which is called the ROC space. The continuous classifier will be represented by a ROC curve: each point belonging to the curve corresponds to a certain threshold, and consequently to a certain binary classifier. So doing, the discrimination threshold can be chosen by observing the classifier's ROC curve, basing on a trade-off between TPR and FPR. In particular, the target is to obtain the highest number of true positives, keeping the number of false positives as low as possible. The ROC curve is a two dimensional measure of the classifier performance. In order to have a scalar measure of it, we can consider the area under the ROC curve (AUC).

4.9.2 Results

As for the previously described attempt, 60% randomly chosen examples from the dataset have been used to build the training set, and the remaining 40% have been used for the test set, in order to evaluate the classification performance. For ANFIS training MATLAB `anfis` routine [34] [69] has been used. In particular, the learning phase of `anfis` simultaneously tunes both antecedent and consequent parameters through a hybrid learning algorithm based on [70]: first the antecedent parameters, related to the membership functions, are determined by the backpropagation gradient descent method, then the

---

[1] Positives stand for oil spills and negatives stand for look-alikes.

[2] Please note that TPR is an approximation to the posterior probability of obtaining a positive classification when the pattern in input is a positive: $TPR \cong p(\mathrm{Y}\,|\,\mathbf{p})$. Analogously, $FPR \cong p(\mathrm{Y}\,|\,\mathbf{n})$.

consequent parameters are computed by means of a least-squares method based on Kalman filter.

In order to provide `anfis` with an initial Fuzzy Inference System structure, data have been partitioned using a fuzzy *c*-means clustering algorithm. So doing, the number of clusters determines the number of rules and the membership functions for the antecedents and consequents in the generated FIS. This number has been chosen by training ANFIS for many times starting from different initial FIS structures, each one obtained by fuzzy *c*-means with a different number of clusters. In particular, 300 fuzzy *c*-means iterations and a fuzziness exponent of 2.0 for the clustering objective function have been used. For each training ANFIS has been run for 300 epochs, then the AUC on the test set has been calculated. In order to reduce random initialization effects, this procedure has been iterated. The number of clusters corresponding to the maximum mean AUC on the test set has been chosen for the final configuration. This number resulted to be 18. Table 8 shows parameters used for ANFIS training and architecture. Figure 14 shows a typical ROC curve obtained from the trained ANFIS on the test set. The mean AUC achieved on the test set is 0.80.

Table 8: Parameters for ANFIS training and architecture.

Number of training epochs	300
Input membership functions	Gaussian
Output membership function	Linear
Learning rate	Adaptive
Learning rate initial step size	0.01
Step size decrease rate	0.9
Step size increase rate	1.1

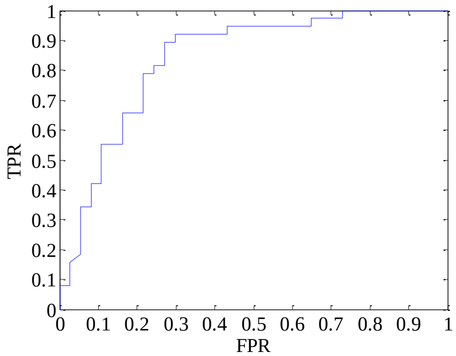

Figure 14: ROC curve for the ANFIS classifier.

4.10 Online cost-oriented classification approach

Once a dataset of oil spills and look-alikes, has been collected, as new satellite images are available and new oil spill candidates are detected, the dataset can be updated, and the classification system can consequently be re-trained, benefiting from a larger dataset. In this framework, an online learning approach allows to easily improve the classification capability of the system. Every time a new satellite image is downloaded and analysed, new candidates detected in the image are included in the dataset and the proposed classification system is able to learn quickly from these new candidates, by means of the online learning process. The described situation well represents an operational scenario where a dataset of oil spills is available, and it is being continuously updated (say daily) by the detection of other oil spills in some new images. These considerations suggested the investigation of an online approach to oil spill classification.

Another important issue is related to desired target conditions. More precisely, since false alarms represent a relevant problem for oil spill classification, it is desirable to assign a different cost to the misclassification errors for each of the two classes. This allows to perform an optimal classification with respect to a chosen cost index for class misclassification, that is, a cost-oriented classification.

According to these considerations, the study of computational intelligence techniques suitable for optical oil spill classification proceeded by combining cost-oriented classification with an online learning approach, which also allowed to use time varying costs and thus to change the desired target conditions (in particular the maximum false alarm rate) according to the latest classification results. In an operational scenario, this means that, for instance, if the coast guard verifies that too many look-alikes have been labelled as real oil spills, then the misclassification cost for the look-alikes, can be increased, thus improving the classification of future events.

The following sections show how to build an online cost-oriented classification system based on an ensemble of SVMs. Then, results obtained by applying this classifier to the oil spill dataset will be shown.

However, we have to consider that the proposed approach meets the requirements of on-line classification, cost oriented classification and of using a suitable performance measure for a two class problem (as will be explained in the following sections) in despite of interpretability. Up to now it has not been possible to include all these four requirements in a single framework, thus the attention will be focused on the first three.

4.10.1 The model

A simple way to tackle a time varying cost scenario is to develop a single cost-oriented classifier, trained over a sliding window, and to dynamically select the optimal trade-off between false positives and negatives, as explained above. So doing, however, one might run into classifier instability.

An empirical method to reduce instability is to employ a meta-classifier, consisting of a set of such cost-oriented classifiers, each one characterized by a static cost, statistically chosen in the initialization phase. Within this set, the best classifier is dynamically selected as the one providing the best trade-off between false positives and negatives, according to the instantaneous classification error index. For the sake of easiness, we assume that the meta-classifier is made of classifiers of the same type. The choice of the specific classifier type (decision trees, neural networks, etc) must consider, first of all, the availability of a cost-oriented training algorithm, and, possibly, the availability of an incremental and decremental training algorithm. In particular, this latter issue significantly improves adaptability, since the training algorithm exploits for each subsequent re-training only the patterns that enter (incremental part) or leave (decremental part) the sliding window, so the system is continuously updated. For this reason, SVMs (Section 3.3) have been chosen, because they meet both requirements, and represent one of the most powerful classification techniques.

More precisely, the cost-oriented formulation of SVMs (CO-SVMs) [39] (Section 3.3.1) and the incremental/decremental formulation of SVMs (ID-SVMs) [40] (Section 3.3.2) have been integrated into a unique framework named COID-SVMs [71]. Then, an ensemble of COID-SVMs, each with its static misclassification error costs has been used. The following sections describe the proposed approach.

4.10.2 Cost-oriented classification in ROC space

This section explains how the ROC space can be used to perform a cost-oriented classification.

As explained in Section 4.9.1, a continuous classifier can be associated with a set of pairs (TPR_τ, FPR_τ), each one corresponding to a certain threshold τ. This allows to evaluate the performance of the continuous classifier in the space (TPR, FPR), that is the ROC space.

Basing on the definition of TPR and FPR, in a two-class cost-oriented classification problem (**p** and **n** for positive and negative classes, respectively) the following cost index is often used:

$$J(TPR, FPR)=FPR\cdot C(\mathrm{Y}, \mathbf{n})\cdot p(\mathbf{n})+(1-TPR)\cdot C(\mathrm{N}, \mathbf{p})\cdot p(\mathbf{p}) \qquad (32)$$

where $C(\mathrm{Y}, \mathbf{n})$ and $C(\mathrm{N}, \mathbf{p})$ are the cost functions associated to the misclassification of, respectively, a negative and a positive pattern, $p(\mathbf{n})$ and $p(\mathbf{p})$ are, respectively, the *a-priori* probabilities for negatives and positives. Such probabilities are typically estimated through the relative frequencies of positives and negatives in the available dataset. Here it is worth noting that the cost functions $C(\mathrm{Y}, \mathbf{n})$ and $C(\mathrm{N}, \mathbf{p})$ must be provided by the user and that they could change over time.

Once a continuous classifier has been trained, the optimal threshold $\bar{\tau}$ can be found by minimizing the cost index J:

$$\bar{\tau} = \arg\min_{\tau_i}(J(TPR(\tau_i), FPR(\tau_i))). \qquad (33)$$

As observed by Provost and Fawcett in [68], in the ROC space the *iso-performance* curves[3] are straight lines when the cost index is the one defined in (32). Thus, a set of costs and

---

[3] *Iso-performance* curves are those curves which connect classifiers having the same performance, that is the same cost index.

class distributions corresponds to a family of iso-performance lines, characterized by the slope:

$$C(\mathrm{Y}, \mathbf{n})\cdot p(\mathbf{n})/C(\mathrm{N}, \mathbf{p})\cdot p(\mathbf{p}). \tag{34}$$

In particular, within a family of iso-performance lines, the line that is tangent to the ROC curve identifies the optimal point on the ROC curve (such point is $(TPR(\bar{\tau}), FPR(\bar{\tau}))$. This allows to conclude that only points laying on the ROC convex hull (i.e. the convex hull of the ROC curve) can be actually optimal. When more continuous classifiers are available, as happens in classifier ensembles, just one convex hull can be computed for all the ROC curves, each curve being associated with one classifier. Figure 15 shows the ROC convex hull of three different ROC curves, and two different optimal points related to different cost index values.

In case of cost-oriented online classification based on an ensemble of continuous classifiers, if the training and the classification processes are performed over a sliding window, the following strategy can be adopted:

1) *train each classifier* over the current window;
2) *draw the ROC curves* by evaluating each trained classifier on a test set and by varying the threshold. Each classifier will produce a single ROC curve;
3) *compute the overall convex hull*, and select the best threshold associated with the best classifier.

Doing this, the optimal classifier and threshold are selected.

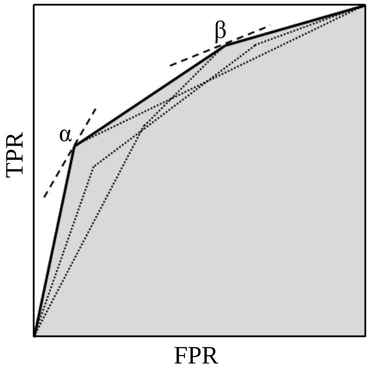

Figure 15: Convex hull of three ROC curves. Lines α and β are two iso-performance lines, both tangent to the convex hull, but with different slopes, thus corresponding to different costs and class distributions.

4.10.3 Repairing concavities in ROC curves

In order to improve the convex hull, a technique presented by Flach and Wu [72] for repairing concavities in ROC curves can be exploited. The basic principle relies on the following observation: classifiers below the ascending diagonal in the ROC space (such as classifiers A and B in Figure 16) perform worse than the random classifier, thus, by simply inverting their predictions, the resulting classifiers will perform better than the random one.

Inverting model predictions means obtaining a true positive rate equal to the complement to 1 of the original true positive rate, and a false positive rate equal to the complement to 1 of the original false positive rate. In the ROC space this corresponds to mirroring the original ROC point through the midpoint on the ascending diagonal. It is worth noting that this operation does not reduce the information content of the classifier. Since the ascending diagonal in the ROC space actually connects two classifiers, that are the classifier always predicting negative (the point in (0,0)) and the classifier always predicting positive (the point in (1,1)), this allows to generalize the prediction inversion procedure to linear segments connecting arbitrary classifiers.

This procedure is known as algorithm *SwapOne* and is illustrated in Figure 17. Classifier 4, built by the algorithm, has:

$$TPR_4 = TPR_1 + TPR_2 - TPR_3$$

$$FPR_4 = FPR_1 + FPR_2 - FPR_3$$

where TPR_i and FPR_i denote the true positive and the false positive rate of classifier i=1,…,4. This can be done if $TPR_1 \le TPR_3 \le TPR_2$ and $FPR_1 \le FPR_3 \le FPR_2$.

If classifiers 1, 2, 3 are obtained by setting different thresholds $\tau_1 > \tau_3 > \tau_2$ on the same continuous classifier, these conditions are automatically satisfied and the algorithm can be applied.

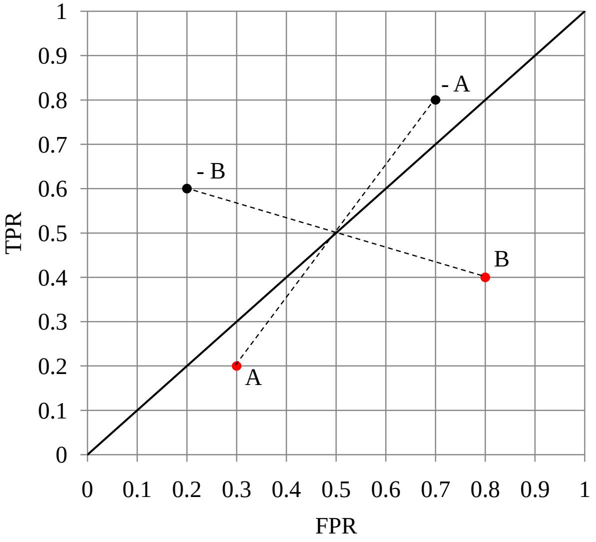

Figure 16: Classifiers A and B perform worse than the random classifier: by inverting their predictions we obtain classifiers -A and -B performing better than the random one.

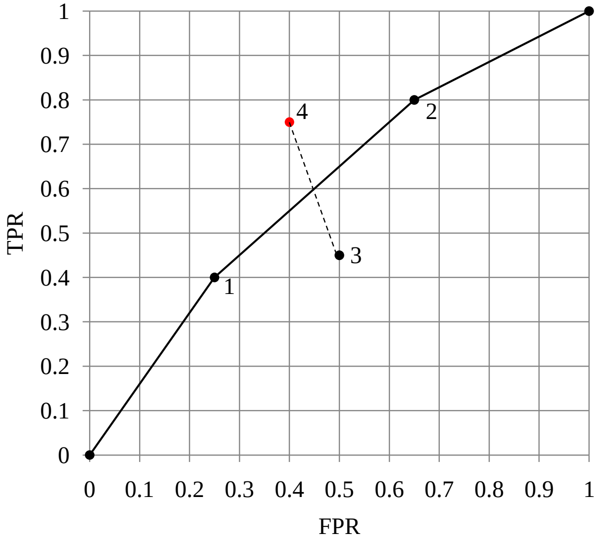

Figure 17: Considering the predictions of classifiers 1 and 2, predictions of classifier 3 are swapped to obtain classifier 4.

Following this approach, the area under the convex hull can sometimes be increased by mirroring points under the convex hull to the other side [72]. This can be achieved because concavities give worse classification performance, thus, by swapping such points, the resulting mirrored points will be located in a more northwest region of the ROC space. Doing so, the ROC curves are modified and the new convex hull is consequently improved. Next section describes the classifiers used to build the ensemble.

4.10.4 COID-SVMs for online classification

The proposed model [71] is a combination between CO-SVMs and ID-SVMs described in Section 3.3.1 and Section 3.3.2, and includes the cost-oriented classification in the ROC space, as described in Section 4.10.2, and the convex hull improvement through concavities repairing (Section 4.10.3). The method starts from the implementation of the ID-SVM by Cauwenberghs and Poggio [40], which has been modified to include cost-oriented classification for unbalanced classes and online classification. Regarding online classification, it is worth pointing out that in the original algorithm by Cauwenberghs and Poggio data acquisition was a batch process, while pattern evaluation was performed incrementally, following the same order as the acquisition. On the other hand, with the online approach, data acquisition happens incrementally, so the SVM structures can be dynamically modified, instead of being fixed by the dimension of the data acquired in batch mode. This intrinsic dynamicity improves the adaptability of the system to time varying conditions.

The online approach is handled by introducing a sliding window over which the training is performed. The use of this window arises from the study of some typical problems of real world applications, such as limited storage capability and continuous incoming data stream, which require the system's update so as to improve the goodness of classification predictions.

In order to build an online training, the algorithm has been structured in the following three steps:

1) *SVM initialization*: this is performed by training the SVM over those patterns belonging to the window. In this way the SVM structure is initialized basing on a small data sample in batch mode. Thus, the resulting SVM trained on the window can be used in incremental mode. In this first step the only difference with respect to the original ID-SVM [40] is that the considered one is cost-oriented.
2) *SVM incremental learning:* a new pattern enters the window and the cost-oriented incremental learning starts.
3) *SVM decremental unlearning:* the oldest pattern exits the window and the decremental unlearning starts.

Besides the online training process, which is built by introducing the sliding window, performance evaluation in ROC space (which implies drawing ROC curves, computing the convex hull, choosing the optimum, improving performance by repairing concavities) requires the presence of a validation set. In addition, performance should be evaluated using a third set, the test set.

In order to integrate all these features, the adopted sliding window has been structured as in Figure 18. The sliding window has a size twice the size of the desired window for learning. Each time, two new elements enter the window and two are excluded from the window. The SVM is trained over the odd elements within the window, while the even patterns compose the validation set, used to evaluate the expected costs, to build the ROC curves and the convex hull, and to repair concavities, if necessary. We can note that this procedure allows only one pattern at a time to enter the training set. The test set is instead chosen outside the window, so that the pattern used for testing are not known by the SVM, thus, the settings established during the validation phase can be evaluated in an independent way. In particular, the test set is composed of a number of patterns following the moving window and equal to the size of the number of elements used for training and for validation. Test set size is thus half of the size of the sliding window.

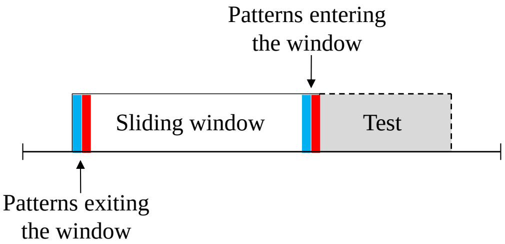

Figure 18: Sliding window used for the online COID-SVM implementation.

The following section explains how the implemented model for online COID-SVM has been included in an ensemble of classifiers.

4.10.5 The ensemble of COID-SVMs in the ROC space

Instead of using just one COID-SVM, with dynamically changing *C*(Y, **n**) and *C*(N, **p**), a set of COID-SVMs has been employed, using static misclassification costs. The advantages associated with this approach are threefold:

- i) an ensemble tends to provide a performance that can outperform the single best classifier;
- ii) an ensemble tends to provide more robust and stable performance;
- iii) static cost functions give better stability to the algorithm used for the SVM online training.

The only drawback is the increase in computational complexity. However, the use of incremental and decremental learning mitigates this problem. Moreover, the computational complexity of the method is negligible if compared to the time needed to download a new satellite image, select, within the image, those regions which could contain possible oil spills, and extract the input features for the classifier. In addition, the classifier is not designed to work in real time conditions, but rather to adapt the classification considering the most recent patterns.

All the COID-SVMs composing the ensemble undergo the training process described in Section 4.10.4, therefore, the validation set is used to draw the ROC curves corresponding to each SVM, and to compute the overall convex hull. This means that the information derived by each classifier are automatically selected by means of the convex hull, and the optimum can be chosen according to the iso-performance line, taking into account all the classifier ensemble. In the same manner the overall concavities can be recovered, allowing for a fusion of the information provided by each classifier, in place of a dynamic classifier selection. Figure 19 shows a flowchart of the proposed classification approach based on the described ensemble of online COID-SVMs in the ROC space.

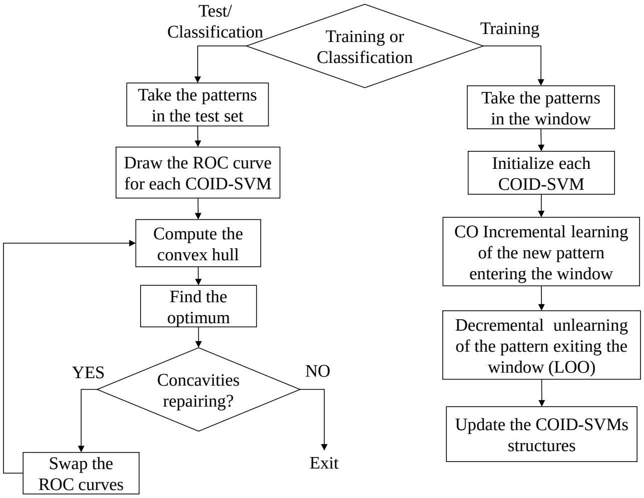

Figure 19: Flowchart of the proposed approach for the classification based on an ensemble of online COID-SVMs.

4.10.6 A software for online cost-oriented classification

The proposed algorithm for building an ensemble of online COID-SVMs, described in Section 4.10.5, has been integrated in a software tool, which is structured following the flowchart in Figure 19. The software is provided with a graphic interface which allows the user to set the inputs and to obtain the optimum for the classification, basing on the convex hull method (see Section 4.10.2). In particular, the user can select the dataset and can set the static misclassification costs for each COID-SVM in the ensemble, the cost functions which define the iso-performance lines, and the size of the sliding window. For each data subset entering the sliding window, the software produces a plot showing the ROC curve for each SVM, the convex hull and the optimum for the classification, all computed over the validation set. Moreover, the cost index $J(TPR, FPR)$, defined in (32) is computed for the ensemble on the validation set and on the test set. The confusion matrix for each SVM can also be computed. Possible concavities in the convex hull can be repaired by enabling the corresponding function.

The software employs an ensemble of five SVMs, namely COID-SVM 1, COID-SVM 2, COID-SVM 3, COID-SVM 4 and COID-SVM 5.

The interface allows to choose the values of the static misclassification costs for the negative and positive class (respectively, $M(\mathrm{Y}, \mathbf{n})$ and $M(\mathrm{N}, \mathbf{p})$) for each COID-SVM in the ensemble. The cost functions $C(\mathrm{Y}, \mathbf{n})$ and $C(\mathrm{N}, \mathbf{p})$ that define the iso-performance lines in the ROC space, used to select the optimum from the convex hull, are also set from the interface. In particular, these cost functions can be either constant or time varying. In the latter case, the symbols $C(\mathrm{Y}, \mathbf{n})(t)$ and $C(\mathrm{N}, \mathbf{p})(t)$ will be used.

The size of the moving window can be selected by means of a sliding bar, while concavities repair is enabled by a checkbox.

In the following the results obtained by applying the online COID-SVM ensemble to the oil spill dataset will be presented, and the effect of repairing convex hull concavities will be investigated.

4.10.7 Online cost-oriented classification results

4.10.7.1 Experiment without concavities repair

Figure 20 shows a typical result for an online classification step. The figure shows the ROC space where the ROC curves for the ensemble of online COID-SVMs are drawn. The violet line represents the overall convex hull and the black line is the iso-performance line tangent to the convex hull. The black squared mark represents the optimum, resulting from the algorithm. In order to find a tradeoff between the size of the dataset (304 elements) and the necessity to test the online learning procedure, a sliding window of 100 elements has been chosen, 50 used for training and 50 for validation. According to Figure 18, each online epoch has been tested on 50 test elements.

Time varying sigmoid cost functions $C(\mathrm{Y}, \mathbf{n})(t)$ and $C(\mathrm{N}, \mathbf{p})(t)$ have been used, with values in the interval [1, 2]. As shown in Figure 21, where the costs are plotted as a function of the online epoch number, $C(\mathrm{Y}, \mathbf{n})(t)$ decreases with time while $C(\mathrm{N}, \mathbf{p})(t)$ increases.

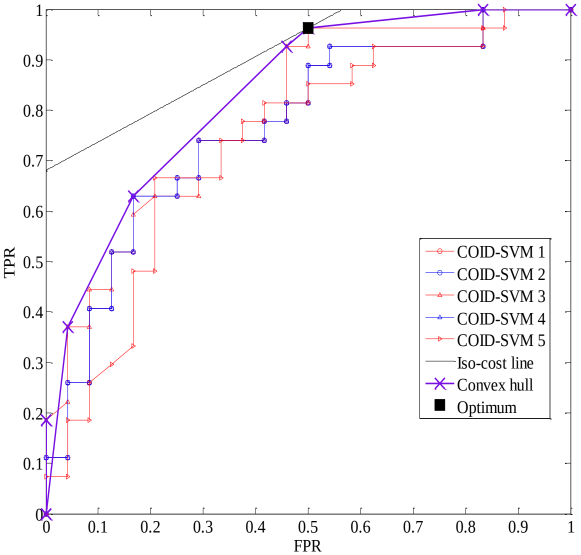

Figure 20: ROC curves for the ensemble of online COID-SVMs. The violet curve represents the convex hull, whereas the black line represents the iso-performance line. The black squared mark is the optimum.

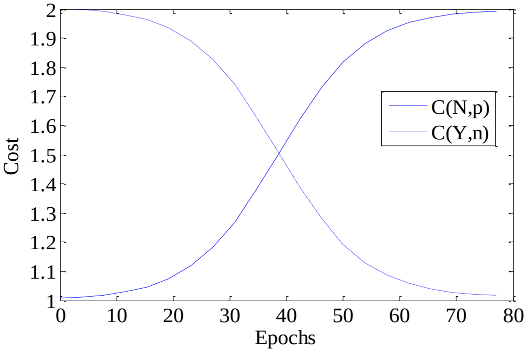

Figure 21: Time varying cost functions C(Y, n)(t) and C(N, p)(t), represented as a function of the online epoch number.

The static misclassification costs associated with each COID-SVM in the ensemble are shown in Table 9. Note that these misclassification costs could assume any value. In particular, for each SVM, $M(\text{Y}, \mathbf{n})$ and $M(\text{N}, \mathbf{p})$ are not necessarily equal. Experimental tests showed that, in this application, using equal misclassification costs for the positive and negative classes, for each COID-SVM, gives better performance. This could be explained with the fact that the oil spill dataset is actually balanced, since the number of elements belonging to the oil spill class is approximately equal to the number of elements belonging to the look-alike class. Indeed, according to the cost oriented formulation of SVMs [39], the static misclassification costs $M(\mathrm{Y}, \mathbf{n})$ and $M(\mathrm{N}, \mathbf{p})$ represent the upper bound on the maximum allowed distance between an element and the separating hyperplane associated, respectively, to the negative class and to the positive class. Thus, using equal values for the two misclassification static costs does not exactly mean that the cost of misclassifying a positive element is being considered equal to the cost of misclassifying a negative one.

Table 9: Misclassification costs associated to each COID-SVM in the ensemble.

	$M(\mathrm{Y}, \mathbf{n})$	$M(\mathrm{N}, \mathbf{p})$
COID-SVM 1	1.0	1.0
COID-SVM 2	1.5	1.5
COID-SVM 3	2.0	2.0
COID-SVM 4	2.5	2.5
COID-SVM 5	3.0	3.0

A measure of the classification performance of the system can be achieved by considering the cost index $J(TPR, FPR)$, defined in (32), computed on the test set[4] at the optimal threshold for the ensemble. However, each online step produces an optimal threshold for the classification of the elements belonging to the current sliding window. This intrinsic dynamicity of the system must be taken into account. In order to obtain a performance index involving the complete dataset, all the cost indexes, each one corresponding to a single online epoch, have been summed over all the online steps, so as to obtain an integrated global cost index for the ensemble applied to the dataset. On the resulting 77 online epochs a global cost index of 92.89 has been obtained on the test set, and of 77.39 on the validation set.

Regarding the mean execution time on the considered dataset, in terms of elapsed CPU seconds, for a single online step this resulted to be 5.52s, on AMD Athlon X2 2.6GHz processor, with 2Gb RAM.

4.10.7.2 Experiment with concavities repair

The application of the technique described in Section 4.10.3 results in a modification of the convex hull, which brings to an increase in the area below the convex hull. In order to estimate the effect of repairing concavities, the corresponding function has been applied at each online step, and the area under the convex hull has been computed. On the 77 online epochs the obtained mean area under the convex hull was of 0.70, while repairing concavities at each online epoch resulted in a mean area under the convex hull of 0.72, thus increasing the area of about 3%. Moreover, the increase in the area corresponds to a decrease in the global cost index of the 2% on the test set and of the 5% on the validation set. Figure 22 shows an example of the effect of repairing concavities in the convex hull. In

---

[4] Note that the optimum is computed by the algorithm on the validation set.

the figure the variation in the area is highlighted in grey, the optimum computed on the improved convex hull is represented by a red squared mark, while the old optimum is represented by a black squared mark. From the theoretical point of view, such an improvement is even more significant, because it demonstrated that combining classifiers provides better results, in this case, than performing a classifier dynamic selection.

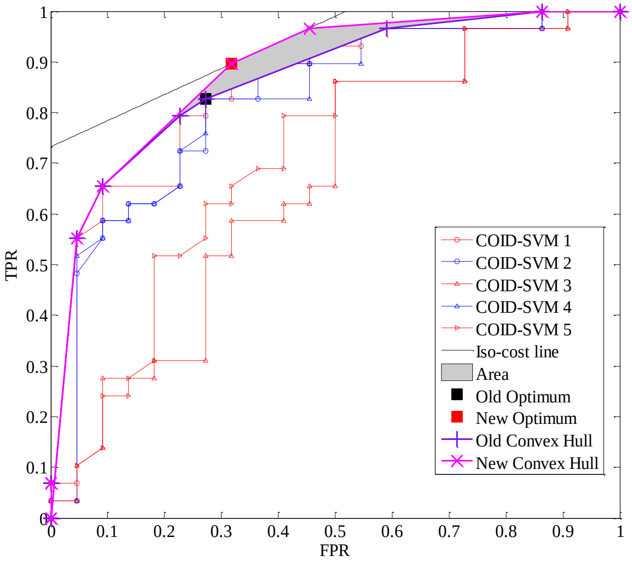

Figure 22: Effect of repairing convex hull concavities.

Chapter Five: Application to bathymetry estimation from optical satellite images

5.1 Motivations

The advent of high resolution satellite sensors (see Table 2) allows to describe the coastal zone with high accuracy, although this implies a reduction of the spectral information. In Chapter 1 we have described how optical satellite data contain contributions from many factors, such as IOPs, bottom depth, bottom spectral properties and atmosphere. The inverse problem of retrieving information on these properties, starting from at sensor spectral radiance values, usually brings to the use of theoretical forward models, as described in Chapter 2. This chapter is focused on the application of a supervised computational intelligence technique to the estimate of sea bottom depth from high resolution optical satellite images, exploiting a dataset of in-situ measured depths. Analytic unsupervised methods rely on many assumptions, but they are able to give indications for an estimated bathymetry map of the area covered by a satellite image. Hybrid methods, based on the use of computational intelligence, combined with simulated datasets, are still affected but many assumptions. On the other hand, if in-situ depth measurements are available, a supervised methodology can be applied, thus allowing to extend the bathymetry information to a much wider area, with high accuracy. This has been the basic motivation for the proposed approach. Moreover, the development of new accurate techniques for producing bathymetric maps from satellite data represents a useful and low-cost support to Rapid Environmental Access (REA) activities, that consist in getting information on hardly accessible zones.

In this chapter a method based on the use of a neuro-fuzzy system, whose input consists only of three spectral bands, is proposed for bathymetry estimation. Situations of limited in-situ data availability are also considered, showing that accurate results are still obtained. In particular, results obtained on two Quickbird images of the same area, acquired in different years and in different meteorological conditions are presented. These two cases allow to study the performance of the presented technique, taking into account the effect of meteorological conditions, and the effect of the reduction of the training set size.

5.2 Overview of bathymetry estimation methods

Bathymetry estimation using remotely sensed images has been widely studied since the 1970’s, when the first empirical models were proposed. One of the difficult aspects of this problem is the effect of variability in the bottom type and in the water column constituents, which are often undistinguishable from changes in bottom depth. If more than a single band is available, some assumptions can be made in order to deal with this aspect. In 1969 Polcyn and Sattinger [73] proposed a two band algorithm for water depth estimation, that assumes that two spectral bands can be found such that the ratio of the reflectance in these two bands is the same for all bottom types within a given scene, and the ratio of water attenuation in these two bands is also constant. This assumption is the base for many semi-empirical methods, such as the two band ratio transform introduced by Lyzenga [74], who proposes a change in the coordinate system, which allows to obtain a variable having a linear dependence on depth.

Empirical methods usually derive water column contributions from adjacent deep waters [75] [76], and assume light attenuation properties to be known *a priori* [75], or empirically derive these properties from the image by regression, using true depths measured on site [77]. Later, semi-empirical methods were developed, like the one proposed in [78], which uses analytical formulae to relate sub-surface reflectance with water column reflectance, albedo and depth, assuming bottom uniformity. However this approach, although more complex than an empirical relationship, does not resolve all the variables of interest.

Bio-optical models were lately developed in order to overcome the need for the knowledge of water properties or in-situ depth measurements. These methods are mostly based on the semi-analytical model proposed in 1999 by Lee *et al.*[17]. This model describes the remote sensing reflectance as a function of the absorption coefficient, the scattering coefficient, bottom reflectance and bottom depth. Only the spectral shape of bottom albedo is assumed to be known. The model produces an estimate of the remote sensing reflectance and iteratively minimizes an error function by comparing the measured reflectance, obtained from a hyperspectral sensor, with the estimated one, finally retrieving optimized parameters representing the water column and bottom contributions. Bio-optical models are able to simultaneously derive bottom depths, albedo and the optical properties of the water column, but must be applied to hyperspectral imagery. If only a few bands are available, such as in the case of the Quickbird sensor, which has 3 bands in the visible and one in the near infrared, these methods cannot be applied.

Adler-Golden *et al.* [79] proposed an algorithm for bottom brightness and depth retrieval, which is similar to the one by Lee *et al.* [17], but it makes the simplifying assumption of constant water optical properties within the scene. This allows to solve some ambiguities in separating the effects of different depths, bottom materials, and water types, and to be applied also to four-channel data, such as data from Quickbird and IKONOS sensors. The algorithm also corrects for spectrally flat reflections from surface glint, foam, and thin clouds, by exploiting one or more infrared channels. It combines atmospheric correction, water reflectance spectral simulations, and a linear unmixing bathymetry algorithm. However, when using Quickbird images no information about water constituents can be retrieved, since only three bands in the visible are available, thus, a pure water model is used. The error on bathymetry calculations results to be around 1 m.

Regarding supervised approaches, some contributions can be found in the literature. In [27] Sandidge and Holyer use a feed-forward fully connected artificial neural network to estimate water depths, ranging from 0 to 6 m, from hyperspectral AVIRIS data. Their neural network is applied to two areas characterized by different water types, bottom types, atmospheric conditions, and illumination levels. The network trained on a combination of the two datasets results in an RMSE of 0.48 m while training on the single datasets gives RMSEs of 0.84 m and 0.39 m, respectively. Results are very accurate but, on the other hand, a large number of training data are used, together with a high number of spectral bands (41). More recently, Grasso *et al.* [80] applied a multilinear regression and a radial basis function artificial neural network to fused data from Quickbird and IKONOS images of the area of Castiglione della Pescaia (Grosseto, Italy), the same area considered in this study. Using the neural network they obtain a standard deviation (STD) of 0.45 m on the test set.

5.3 Two case studies

In this study two multi-spectral high resolution images of the same area, acquired in different years and in different meteorological conditions have been used. In particular, the first one has been acquired in calm sea conditions, and is supplied with a large dataset of in-situ measured depths for training and validation of the method. The second image has been acquired in slight sea conditions and is supplied with a limited dataset of in-situ measured depths, collected along two transects within the scene.

The two images have been acquired by the multi-spectral sensor on board Quickbird commercial satellite. Table 10 reports Quickbird specifications, among which the most interesting one is the spatial resolution, that is 2.44 m for multi-spectral data. Four spectral bands are available, three in the visible and one in the NIR (see Table 11).

Table 10: Quickbird specifications.

Orbit Altitude	450 km
Orbit Inclination	97.2 deg., sun-synchronous
Speed	7.1 km/s
Equator Crossing Time	10:30 a.m. (descending node)
Orbit Time	93.5 min
Revisit Time	1-3.5 days depending on latitude
Swath Width	16.5 km at nadir
Quantization	11 bits
Spatial Resolution	Panchromatic: 61 cm (nadir) Multi-spectral: 2.44 m (nadir)

Table 11: Quickbird multi-spectral bands

Band	**Bandwidth** (nm)
Blue	450-520
Green	520-600
Red	630-690
NIR	760-900

Both images are related to the area of Castiglione della Pescaia (Grosseto, Italy), a touristic locality of great interest, but they have been acquired in different dates: the first image (Figure 23 (a)) has been acquired on April 27th, 2007 at 10:32 UTC, while the second one (Figure 23 (b)) has been acquired on July 14th, 2008 at 10:32 UTC. We will refer to the analysis of these two images as *Castiglione* 2007 *case* and *Castiglione* 2008 *case*.

The information about date and acquisition time is necessary in order to estimate tide effects and thus refer depth data to mean sea level used as a standard in cartography. In this work all data are referred to the average sea level measured in Genoa (Italy) using the ancient Thompson tide gauge.

In order to train and validate the algorithm, in-situ truth data have been used, that have been collected by the Istituto Idrografico della Marina (IIM) during two hydrographic surveys conducted, respectively, in June 2007 for the *Castiglione* 2007 *case* and in September 2008 for the *Castiglione* 2008 *case*. These data have been acquired by means of a multi-beam echo sounder whose accuracy on depth measurement was of 0.01 m, and are referred to the average sea level measured in Genoa.

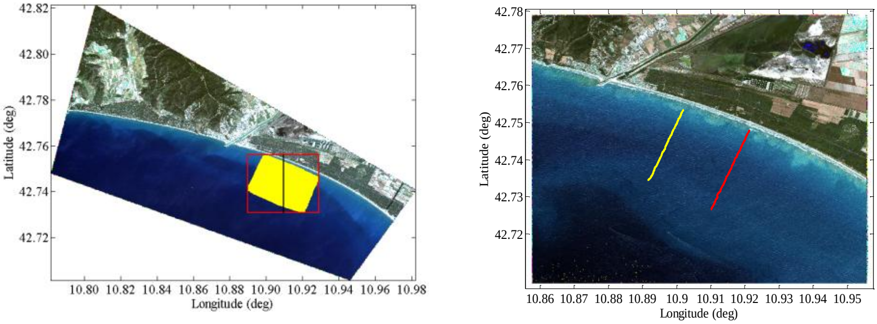

(a) (b)

Figure 23: (a) Quickbird image (RGB) of the area of Castiglione della Pescaia (Grosseto, Italy), acquired on April 27th, 2007 at 10:32 UTC. The red square represents the bounding box enclosing the area covered by in-situ depth measurements, which are represented as yellow dots. The black line represents a test transect. (b) Quickbird image (RGB) of a subset of the same area, acquired on July 14th, 2008 at 10:32 UTC. In-situ measurements have been acquired along two transects, represented as yellow and red dots, respectively.

As can be observed from Figure 23 (a) and Figure 23 (b) there are some differences between the two cases. First, in the *Castiglione* 2007 *case* the image has been acquired in optimal meteorological conditions, in terms of clear sky, good horizontal visibility and scarce sea surface roughness, while in the *Castiglione* 2008 *case*, although the visibility is still good and the sky is cloudless, the sea surface roughness is much more important, and there is presence of foam not only close to the shoreline but also in deeper waters. Second, the in-situ depth measurements available for the *Castiglione* 2008 *case* are represented by two transects in the image (yellow and red dots in Figure 23 (b)), while those available for the *Castiglione* 2007 *case* cover a much larger area which can be enclosed in a bounding box (the red square in Figure 23 (a)). Finally, the scene represented in the 2008 image corresponds approximately to the bottom right quarter of the 2007 image.

In the pre-processing phase of the analysis each image has been first georeferenced, then land pixels have been identified and removed by applying a mask based on a threshold on the NIR band. Pixels affected by the presence of foam close to the shoreline have also been identified and removed by applying a mask based on a threshold on the red band of each image. Finally, a median filter has been applied in order to reduce the variation of the surface reflectance due to wind waves on the sea surface. The appropriate kernel dimension for the filter has been chosen by evaluating performance as a function of kernel dimension, as will be described in detail later on.

5.4 A neuro-fuzzy approach to bathymetry estimation

Supervised regression for the estimation of sea bottom depth can be tackled in very different ways, ranging from white models, like parametric analytical models, both linear and nonlinear, to black-box models (like artificial neural networks). The former can be better understood, but it is generally difficult to chose the appropriate parametric model for the particular application. On the contrary, black-box models based on artificial neural networks have the advantage of being general purpose scalable models, that can be used on a large number of applications. However, they tend to lack of interpretability (the parameters learned during training, like the weights on the inputs of each neuron, do not have a clear meaning). For this application to bathymetry estimation neuro-fuzzy models have been chosen, because they combine the powerful learning algorithm of neural networks with the interpretability of fuzzy systems. In particular, an ANFIS [34] (see Section 3.2) has been adopted. Unlike what has been described in Section 4.9, where a two-class classifier for oil spill classification was needed, here ANFIS can be regarded as a nonlinear regression technique.

The choice of ANFIS arises from many motivations. First of all, adaptive networks allow to design a model without using any predetermined knowledge of the problem. More precisely, traditional fuzzy inference systems need a rule structure and membership functions which are predetermined by the user, on the basis of his previous knowledge and interpretation of the variables involved in the problem. On the other hand, adaptive networks use a collection of input-output data pairs in order to determine the model structure. In particular, these networks use the supervised learning procedure to adapt the membership functions to the input variable characteristics, which are thus derived from the dataset. Beside this feature of adaptive networks, another advantage of using ANFIS is represented by interpretability, which is indeed preserved. While neural networks are black-box models, ANFIS can be regarded as a grey-box model, since it allows to describe the problem starting from data, without going into details but keeping interpretability into account. Some parameters must still be provided, however, these are quite easy to set.

Another advantage of using ANFIS is that is it already available in the MATLAB Fuzzy Logic Toolbox [69].

The three radiance bands of the image corresponding to wavelengths centred in the visible spectrum have been used as input for the fuzzy inference system. The output of the system represents the estimated bottom depth, while in-situ measured depth represents the desired output from the system, that is the target. For each image, in order to build a dataset composed by the system input and corresponding output, pixels where in-situ measurements were available have been selected. Thus, each selected pixel corresponds to an element in the data set, composed of a pair $\{[L_1, L_2, L_3], d_m\}$, where $[L_1, L_2, L_3]$ is the radiance vector and d_m is in-situ measured depth corresponding to the pixel.

In the following, the results achieved by applying ANFIS to the two available Quickbird images will be separately discussed for *Castiglione* 2007 *case* (Section 5.4.1) and for *Castiglione* 2008 *case* (Section 5.4.2).

5.4.1 Experimental results: Castiglione 2007 case

Figure 24 shows the in-situ depth measurements available for the *Castiglione* 2007 *case*: each pixel in this figure represents a value of in-situ measured depth d_m which has been used to build the dataset pairs.

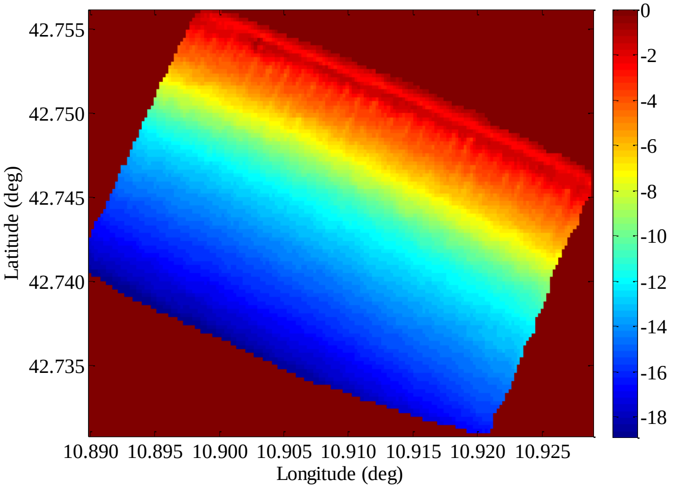

Figure 24: Castiglione 2007 case: in-situ measured depth.

As mentioned in Section 5.3, during the pre-processing phase the image has been filtered by means of a median filter. In order to choose the optimal kernel dimension for the filter, performance has been evaluated as a function of kernel dimension, in terms of STD over the entire depth range. In particular, as Table 12 shows, performance obtained using a kernel dimension of 3×3, 5×5, 7×7, 9×9, 11×11 and 17×17 pixels, have been evaluated. One third of the elements randomly chosen from the complete available dataset was used as a test set for the STD calculation, while one of the remaining thirds was used for ANFIS training and the other one for ANFIS validation. In this preliminary study on the optimal dimension for the kernel filter a grid partitioning approach has been used for the initialization of ANFIS. This choice is motivated by the fact that when using a uniform grid partition for the inputs only the number of fuzzy sets for each input variable must be specified, and no further parameter setting is required. In particular, 5 fuzzy sets were used for each input variable, so as to obtain 125 fuzzy rules, which is a reasonable number even in the case of 17×17 filtering window, that is the case for which there is a lower number of elements in the dataset (due to the lower resolution of the map).

For ANFIS training MATLAB `anfis` routine [34] [69] has been used, with the same hybrid learning algorithm based on [70] and described in Section 4.9.2. Overfitting has been prevented by the presence of a validation set. ANFIS has been trained for 300 epochs, adopting Gaussian membership functions for the inputs and a linear membership function for the output. For the backpropagation algorithm an adaptive learning rate has been chosen, with an initial step size of 0.01, a step size decrease rate of 0.9, and a step size increase rate of 1.1.

Table 12 reports the STD calculated on the test set. These values are mean values obtained by running the algorithm many times for each filtering window. Best results are obtained using a kernel dimension for the filter of 9 × 9 pixels. This can be also observed from Figure 25, which shows a plot of the mean STD obtained on the test sets as a function of the kernel dimension for the filter. In the figure the minimum STD, corresponding to a kernel of 9 × 9 pixels, is highlighted by a black cross. In the following all the results will refer to the image at this resolution.

Table 12: STD obtained using the supervised method on the 2007 image where different median filters were applied

Kernel dimension for the filter	STD (m)
3 × 3	0.67
5 × 5	0.52
7 × 7	0.41
9 × 9	0.38
11 × 11	0.75
17 × 17	1.04

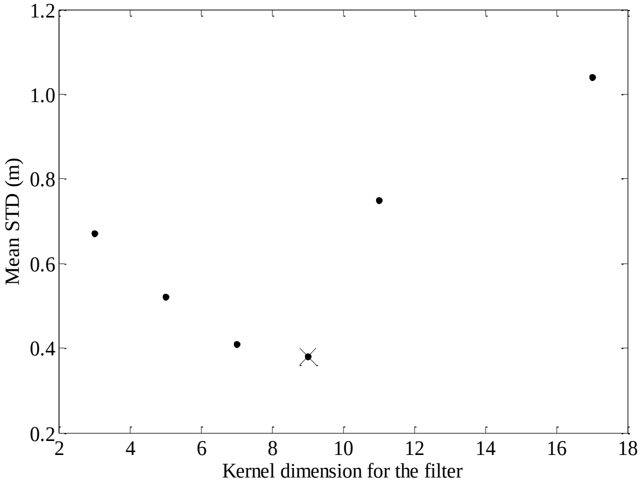

Figure 25: Castiglione 2007 case: mean STD obtained on the test sets as a function of the kernel dimension for the filter. In the plot the minimum STD, corresponding to the chosen kernel of 9 × 9 pixels, is highlighted by a black cross.

The following sections (5.4.1.1 and 5.4.1.2) describe the results obtained by applying ANFIS to the 2007 Quickbird image in two different experiments.

5.4.1.1 Experiment S-U

For the first experiment the data set has been randomly split into three subsets, composed, respectively, of 3623, 3602 and 3615 elements. The first one has been used as a training set while the second one has been used as a validation set, whose task is to prevent over learning and to maintain the network's generalization ability. The third set has been used as a test set in order to evaluate the identification capabilities of the algorithm. In the following this experiment will be referred to as *Experiment S-U*, where *S* indicates that the method is supervised and *U* indicates a uniform random partition of the data set in three sets.

Borrowing the term from time series prediction nomenclature [81], it is worth pointing out that this procedure consists in an *in-sample* methodology, since the examples used for the validation are chosen randomly from the same set as the examples used for the training.

As introduced in Section 5.4, MATLAB `anfis` routine has been used for ANFIS training, adopting the above mentioned hybrid learning rule. For the gradient descent algorithm an adaptive learning rate has been used with an initial step size of 0.01, a step size decrease rate of 0.9, and a step size increase rate of 1.1. For the consequent least square estimate Kalman filter has been used.

In order to provide `anfis` with an initial Fuzzy Inference System structure, data have been partitioned using a fuzzy *c*-means clustering algorithm. Although a grid partitioning consists in practice in a non parametric technique, fuzzy *c*-means clustering has been chosen because input data distribution resulted not to be uniform.

The number of clusters has been chosen by training ANFIS for many times, starting from different initial fuzzy inference system structures, each one obtained by fuzzy *c*-means with a different number of clusters. For the fuzzy *c*-means algorithm 300 iterations and a fuzziness exponent of 2.0 for the clustering objective function have been used. For each training ANFIS has been run for 300 epochs, and the errors on training, validation and test sets have been computed. In order to reduce random initialization effects, this procedure has been iterated, and the mean errors on the training, validation and test sets have been computed. Then, the number of clusters corresponding to the minimum mean error on the validation set, has been chosen. As Figure 26 shows, this number resulted to be 32.

The number of clusters determines the number of rules and the membership functions for the antecedents and consequents in the generated FIS. Regarding other settings for ANFIS architecture, Gaussian input membership functions and a linear output membership function have been employed.

After the preliminary setting phase ANFIS has been trained for 300 epochs and performance obtained on training, test, and on a transect dividing the considered bounding box in two (shown in Figure 23(a)) have been evaluated. Averaging the results of multiple runs (in order to consider fluctuations due to ANFIS initialization) mean STDs of 33.8 cm on the training set, of 36.7 cm on the test set, and of 28.3 cm on the transect, have been obtained, which is a good result. Moreover, this result is also more accurate than those achieved with other supervised methods (such as artificial neural network-based). For instance, Grasso *et a.l.* [80] obtained a STD of 45 cm on the test set by applying a radial basis function artificial neural network to fused data from Quickbird and IKONOS images of the same area considered in this study.

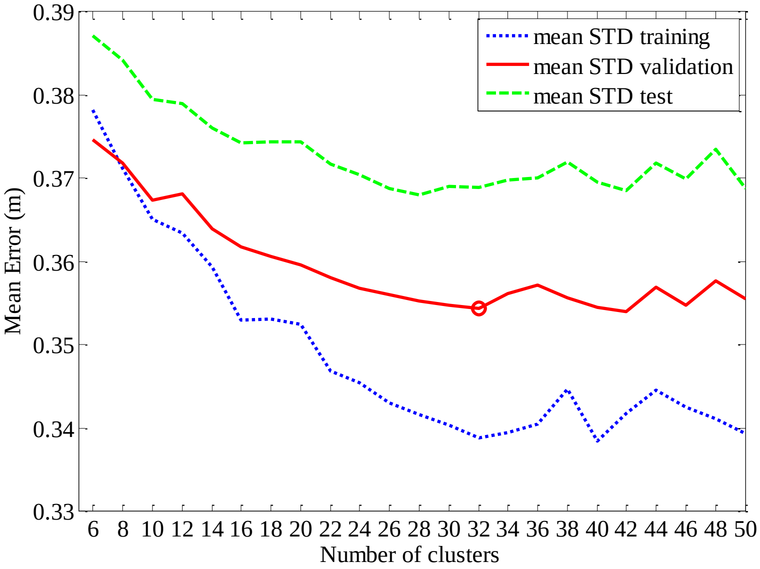

Figure 26: Experiment S-U: mean STD on training (blue dotted line) validation (red solid line) and test (green dashed line) sets for different number of clusters. The chosen number of clusters (32) corresponding to the minimum mean STD on the validation set is highlighted in the figure by a red circle.

Figure 27 shows a scatter plot of the depth estimated by ANFIS vs. the in-situ measured depth, for the training set and for the validation set. Figure 28 shows the same plot for the test set, and an additional plot which represents the estimated and the in-situ measured depth (respectively the solid line and the dashed line) along the transect dividing the considered bounding box in two. The latter plot allows to see how the bottom profile is represented by the network. The model fits well the data, since the value of the coefficient of determination R^2 is 0.995 for training, validation and test sets, and this represents a measure of the goodness of fit.

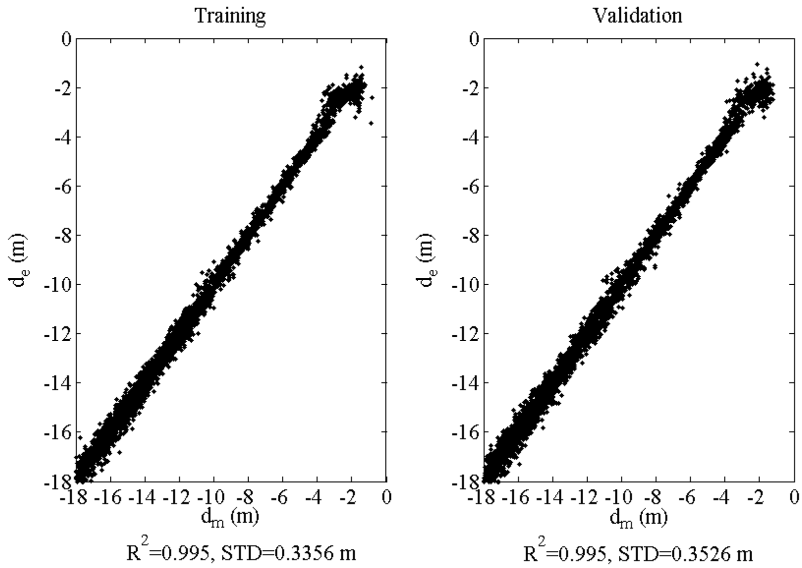

Figure 27: Experiment S-U: scatter plot of depth estimated by ANFIS vs. in-situ measured depth for the training set (left) and for the validation set (right).

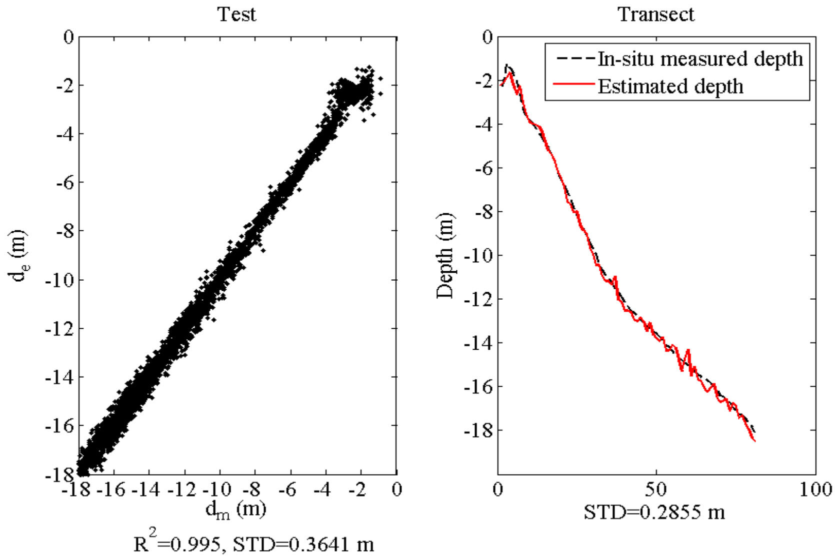

Figure 28: Experiment S-U: scatter plot of depth estimated by ANFIS vs. in-situ measured depth for the test set (left). Estimated and in-situ measured depth for the validation set (respectively solid line and dashed line) along the transect dividing the considered bounding box in two (right).

Performance have been then evaluated as a function of depth. In particular, transect estimated depth has been ordered by the corresponding in-situ measured depth and the cumulative STD has been computed as a function of depth. The cumulative STD for depth D can be written as follows:

$$STD_D = \sqrt{\sum_{i=1}^{N_D} \left(d_e^i - d_m^i\right)^2 / N_D} \ . \tag{35}$$

where N_D is the number of data having in-situ measured depth less than D, while d_e and d_m are, respectively, the estimated and the in-situ measured depth.

Figure 29 shows a plot of the cumulative STD as a function of the in-situ measured depth absolute value. As it is evident from the figure, the error tends to be constant around 0.27 m for $|d_m|$> 8 m and is always below 0.40 m for $|d_m|$< 8 m.

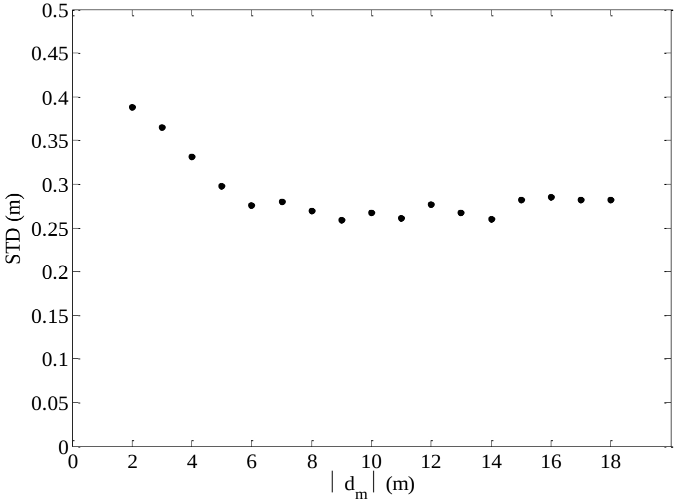

Figure 29: Cumulative STD as a function of the absolute value of in-situ measured depth, obtained by ANFIS in the Castiglione 2007 case.

5.4.1.2 Experiment S-P1, S-P2, S-P3, S-P4

In practice, a bathymetric survey which covers an area as big as the considered bounding box is quite expensive in terms of time and costs. A more realistic situation is represented by a bathymetric data collection performed by a drift boat, released by a vessel, going along a closed path. Thus, some experimental tests have been carried on by simulating such a limited in-situ data availability through four different closed paths, built within the area covered by the presence of in-situ data. Figure 30, Figure 31, Figure 32 and Figure 33 show the four paths, namely path 1 (P1), path 2 (P2), path 3 (P3) and path 4 (P4), composed, respectively, of 616, 722, 753 and 544 elements. In each figure black pixels are those belonging to the path. In the following, these experiments will be called as *Experiments S-P*1, *S-P*2, *S-P*3, *S-P*4, where *S* stands for supervised and *P*1, *P*2, *P*3, *P*4 indicate the different paths. Radiance vectors of the selected pixels, coupled with the corresponding in-situ measured depths, have been used to build four different datasets for ANFIS training and validation. More precisely, each path has been randomly divided into two halves: one for the training and one for the validation phase. The purpose of these experiments is to evaluate ANFIS performance in a situation of limited training data availability.

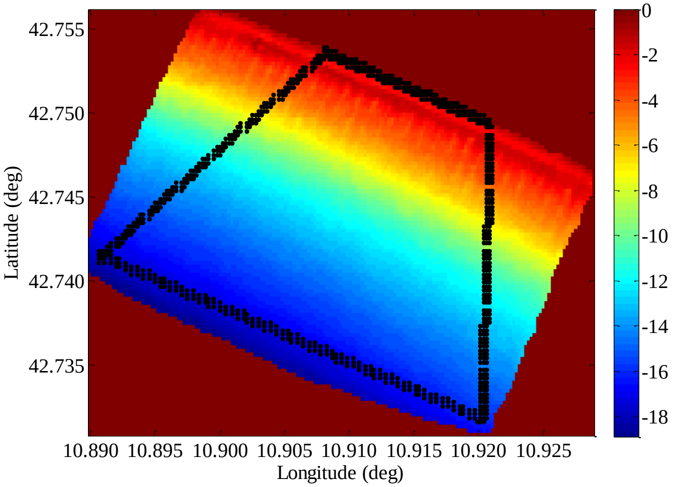

Figure 30: Path P1, black pixels are those belonging to the path.

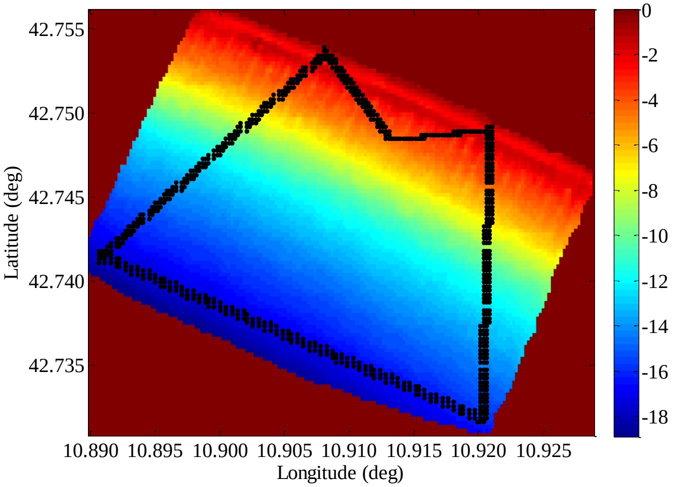

Figure 31: Path P2, black pixels are those belonging to the path.

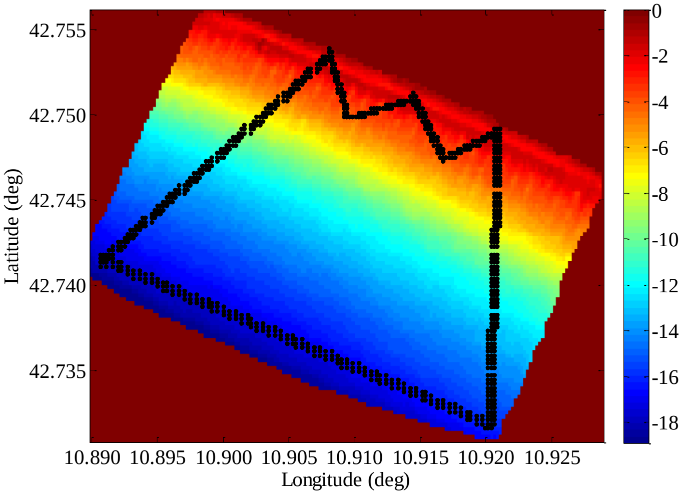

Figure 32: Path P3, black pixels are those belonging to the path.

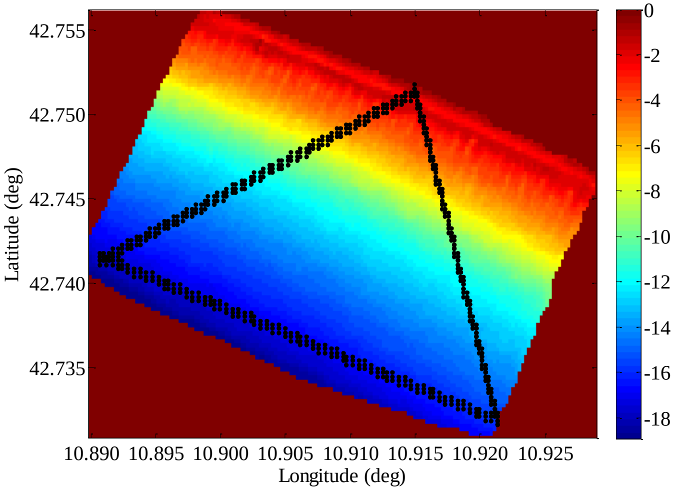

Figure 33: Path P4, black pixels are those belonging to the path.

Results obtained from each of these different ANFIS training processes, have been evaluated by using as test set the same subset composed of 3615 elements as before. This has been done in order to compare the performance obtained by training on different data sets; in particular this allows the comparison with *Experiment S-U* results.

As the validation carried out for *Experiment S-U* has been defined an in-sample validation, the procedure used for *Experiments S-P*1, *S-P*2, *S-P*3, *S-P*4 can now be defined an out-of-sample validation, since in this case test data are chosen among the elements belonging to a set which is different from that used for training.

Since in the case of out-of-sample validation the network's generalization capability is the main issue, the number of clusters used by the fuzzy *c*-means clustering algorithm has been reduced. In particular, the study performed in *Experiment S-U* for the optimal number of clusters choice, has been repeated. This number resulted to be 5, and it has been used for all of the four paths, since the number of elements of the four corresponding training sets is not significantly different (if compared to the number of elements of the training set used in *Experiment S-U*).

It can be observed that the number of clusters obtained in this experiment (5) is significantly lower than that found in *Experiment S-U* (32). This can be due to several reasons: first, in this case the network is asked to perform an out-of-sample generalization instead of an in-sample one. Second, the training set is much more limited than in the previous case, whereas the test set is the same. For these reasons, the procedure produces a lower number of clusters, which implies a worse performance on the training set but that allows, on the other hand, to generalize quite well on the entire image. Using a greater number of clusters (say 32, like in the *Experiment S-U* case) leads to obtain a better performance on the training set but a lower one on the validation and test sets, which means a lower generalization capability.

Table 13 shows the results of *Experiments S-P*1, *S-P*2, *S-P*3, *S-P*4. The table shows the errors obtained on each training set, on the test set and on the vertical test transect. The values are obtained by averaging the results of multiple runs with the same configuration of ANFIS, in order to consider fluctuations due to ANFIS initialization. Regarding the training, the same settings as those adopted in *Experiment S-U* have been used. The best performance is obtained using path P3, which achieves an STD of 0.45 m on the test set (see Figure 34 and Figure 35 for scatter plots). The worst performance is obtained using path P4, which obtains an STD of about 0.63 m on the test set.

If it is possible to plan the bathymetric survey, the results shown in this section can give some suggestions. According to these results, a bathymetric data collection performed by a drift boat, released by a vessel, and going along a closed path, will produce more accurate bathymetry estimate if a path shaped such as path P3 is chosen, instead of a path like path P4, since this allows to span all depths in the area of interest collecting a limited number of measurements. In particular, it can be worth sampling more the region close to the shoreline.

Table 13: Results of Experiments S-P1, S-P2, S-P3, S-P4. The errors obtained on each training set, on the test set and on the vertical transect are shown. The values are obtained by averaging results of multiple runs with the same configuration of ANFIS

Experiment	**Mean STD on training set (m)**	**Mean STD on test set (m)**	**Mean STD on transect (m)**
*S-P*1	0.294	0.512	0.583
*S-P*2	0.331	0.470	0.499
***S-P*3**	**0.378**	**0.452**	**0.431**
*S-P*4	0.289	0.627	0.473

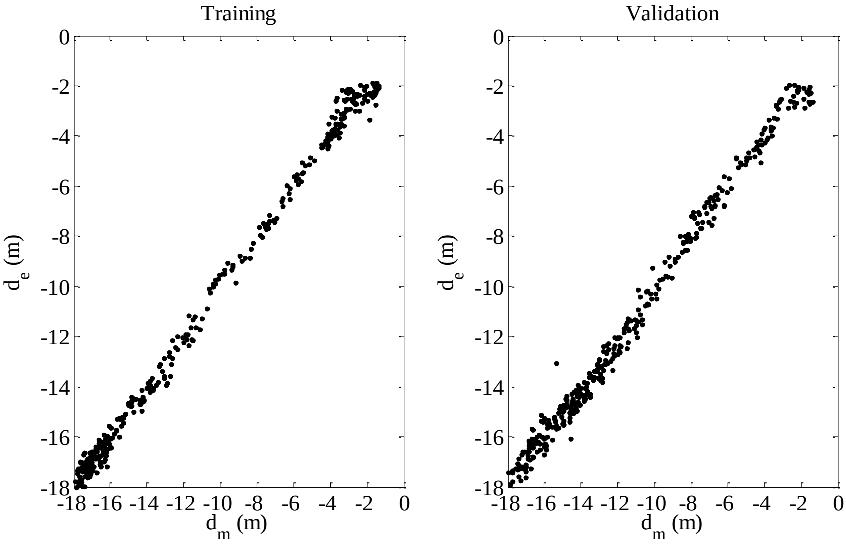

R^2=0.996, STD=0.3783 m

R^2=0.991, STD=0.4568 m

Figure 34: Experiment S-P3: scatter plot of depth estimated by ANFIS vs. in-situ measured depth for the training set (left) and for the validation set (right).

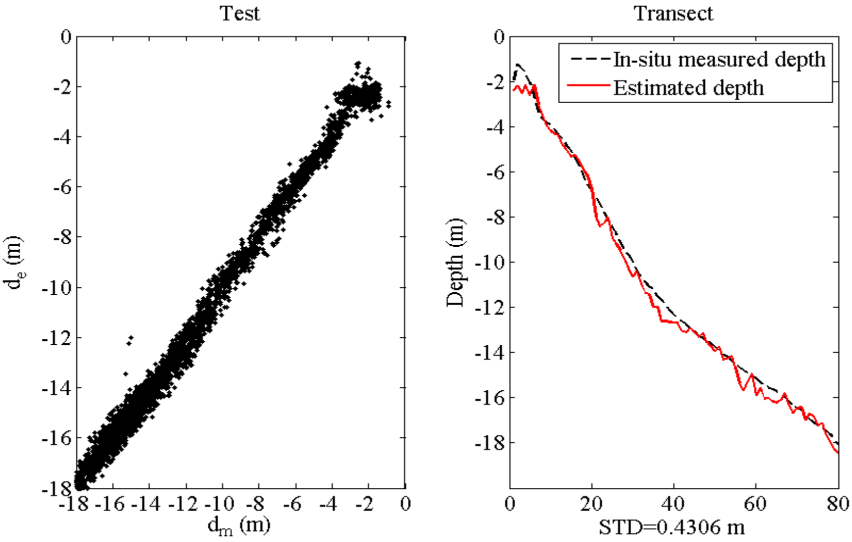

R^2=0.992, STD=0.4519 m

STD=0.4306 m

Figure 35: Experiment S-P3: scatter plot of depth estimated by ANFIS vs. in-situ measured depth for the test set (left). Estimated and in-situ measured depth (respectively the solid line and the dashed line) along the transect dividing the considered bounding box in two and for the validation set (right).

5.4.2 Experimental results: Castiglione 2008 case

The application of the supervised method to *Castiglione* 2008 *case* allows to validate the method in case of limited in-situ data availability. Only two sets of in-situ measured depths, laying along two transects, are available and can be used to build the training, validation and test sets for ANFIS. These two transects are represented in Figure 23 (b): *Transect* 1 is represented in yellow and *Transect* 2 is represented in red.

Transect 1 has been used as a test set, while *Transect* 2 has been randomly split in two parts to be used one for the training and one for the validation phase. Thus, 267 elements have been used for the training set, 241 elements for the validation set, and 143 elements for the test set.

It can be noted that this analysis can be regarded as an out-of-sample validation, like the one performed in *Experiments S-P*1, *S-P*2, *S-P*3, *S-P*4 (Section 5.4.1.2). The only difference is in the size of the test set.

In the pre-processing phase a median filter with 11×11 kernel dimension has been applied. Then, analogously to what done for *Castiglione* 2007 *case*, the optimal number of clusters for the fuzzy *c*-means algorithm has been selected, and this number resulted to be 5. As regards the training, the same settings as those adopted in *Experiment S-U* and *Experiments S-P*1, *S-P*2, *S-P*3, *S-P*4 have been used. In this case, due to the unfavourable sea conditions in terms of sea surface roughness in the scene, signal to noise ratio was significantly reduced, thus, depth estimate has been limited to depths above −14 m, since signal to noise ratio decreases in deeper waters.

On the test a mean STD of about 0.64 m has been achieved. This result is consistent with those obtained in *Experiments S-P*1, *S-P*2, *S-P*3, *S-P*4, also considering that in this case the size of the training set is significantly smaller, and the sea surface roughness is greater.

Figure 36 shows the scatter plot of depth estimated by ANFIS vs. in-situ measured depth for the test set, and the comparison between estimated and in-situ measured depth along the test transect, that is *Transect* 1. *Castiglione* 2008 *case* shows how limited data availability together with unfavourable sea conditions limit depth estimate to a smaller range, still giving accurate results.

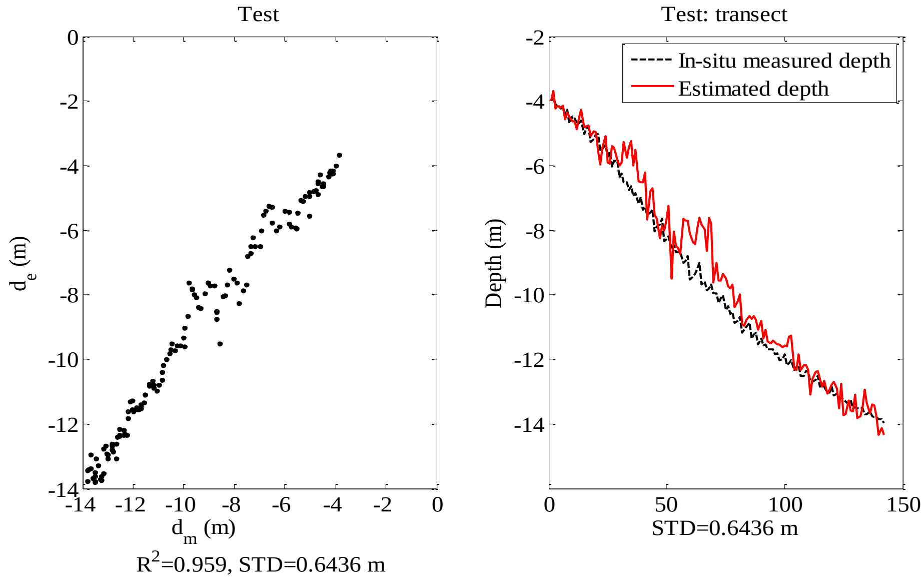

Figure 36: Castiglione 2008 case: scatter plot of depth estimated by ANFIS vs. in-situ measured depth for the test set, that is Transect 1 (left). Estimated and in-situ measured depth (respectively the solid line and the dashed line) along Transect 1 (right).

Chapter Six: Conclusions

In this thesis computational intelligence techniques have been applied to remotely sensed optical data for applications in the field of marine and coastal environmental monitoring.

The thesis contains a number of original and new contributions. First of all, the use of a significant dataset of oil spills, collected in satellite multi-spectral images for the oil spill classification problem, represents a novelty. While SAR-based oil spill detection services have already been adopted by environmental protection authorities for operational monitoring, only few studies have been presented in the literature regarding oil spill classification from optical data. Moreover, these studies mainly use empirical relationships obtained on few single cases. Thus, the extensive study that has been carried on about different type of classifiers, and the exploitation of a significant dataset of oil spills detected in satellite optical images, bring an innovative contribution to the oil spill classification problem. In addition, batch and online learning approaches have been experimented in this thesis, while in the literature only batch approaches have been employed for similar problems. Results show the big potential of optical images for oil spill classification based on intelligent classifiers, and the feasibility of such an approach for operational monitoring activities.

The second major innovative contribution in this thesis is the application of ANFIS to bathymetry estimation from high resolution multi-spectral images. Beside the choice of the classifier, the overall approach, which is purely experimental, is innovative for this field. Most studies regarding the estimation of sea bottom depth in fact rely on theoretical models of apparent optical properties of the water body, either through semi-empirical methods, implicit methods, or through the use of simulated training dataset for supervised classification algorithms. On the other hand, in this thesis the algorithm is trained only on real data, and no model-based assumptions are used, thus avoiding any related systematic uncertainties. In case of optimal sea conditions (low sea surface roughness) and significant training set size, results obtained with ANFIS outperform previous works on other computational intelligence techniques applied to bathymetry estimation. In case of unfavourable sea conditions (slight sea), and limited training dataset, results are still accurate, and comparable with the others. Moreover, the indications on optimal paths for data collection could represent a useful support for bathymetric survey planning activities, showing that regions closer to the shoreline deserve a higher sampling with respect to deeper waters.

In conclusion, this thesis proposes some innovative and feasible approaches for the combination of optical data and computational intelligence techniques in the remote sensing of the marine and coastal environment.

References

[1] Central Intelligence Agency, "CIA- The world fact book," ISSN 1553-8133, Retrieved on October 6, 2010 https://www.cia.gov/library/publications/the-world-factbook/geos/xx.html#Geo.

[2] Gordon, H. R., and Morel, A., "Remote assessment of ocean color for interpretation of satellite visible imagery. A review," Lecture Notes on Coastal and Estuarine Studies, Springer-Verlag, New York, 114 pp., 1983.

[3] Rossow, W. B., Kinsella, E., Wolf, A., and Gardner, L., "Description of reduced resolution radiance data," WCRP/ISCCP, WMO/TD No. 58, 132 pp., 1985.

[4] Prieur, L. and Sathyendranath, S., "An optical classification of coastal and oceanic waters based on the specific spectral absorption curves of phytoplankton pigments, dissolved organic matter, and other particulate materials," Limnol. Oceanogr., vol. 26, pp. 671-689, 1981.

[5] IOCCG, "Remote sensing of ocean colour in coastal, and other optically-complex, waters," Reports of the International Ocean-Colour Coordinating Group, No. 3, Sathyendranath, S. (ed.), IOCCG, Dartmouth, Canada, 140 pp., 2000.

[6] Morel, A., and Prieur, L., "Analysis of variations in ocean color," Limnol. Oceanogr., vol. 22, pp. 709-722, 1977.

[7] Morel, A., and Gentili, B., "Diffuse reflectance of oceanic waters: Its dependence on Sun angle as influenced by the molecular scattering contribution," Appl. Opt., vol. 30, pp. 4427-4438, 1991.

[8] Morel, A., and Gentili, B., "Diffuse reflectance of oceanic waters. II. Bidirectional aspects," Appl. Opt., vol. 32, pp. 6864-6879, 1993.

[9] Preisendorfer, R. W., "Hydrologic optics. Vol. I. Introduction," U. S. Department of Commerce National Oceanic and Atmospheric Administration, Environment Research Laboratory, Honolulu, 218 pp., 1976.

[10] Mobley, C. D., "Light and water: radiative transfer in natural waters," Academic Press, San Diego, CA, 592 pp., 1994.

[11] Mobley, C. D., and Sundman, L. K., "Hydrolight 4.1 Users' Guide", Sequoia Scientific, Mercer Island, WA, 2000.

[12] Carder, K. L., Chen, F. R., Lee, Z. P., Hawes, S. K. and Kamykowski, D., "Semianalytic Moderate-Resolution Imaging Spectrometer algorithms for chlorophyll a and absorption with bio-optical domains based on nitrate- depletion temperatures," J. Geophys. Res., vol. 104, pp. 5403-5421, 1999.

[13] Lee, Z., Carder, K. L., Mobley, C. D., Steward, R. G. and Patch, J. S., "Hyperspectral remote sensing for shallow waters. I. A semianalytical model," Appl. Opt., vol. 37, pp. 6329-6338, 1998.

[14] Lee, Z., Carder, K. L., and Arnone, R. A., "Deriving inherent optical properties from water color: a multiband quasi-analytical algorithm for optically deep waters," Appl. Opt., vol. 41(27), pp. 5755-5772, 2002.

[15] Hoogenboom, H. J., Dekker, A. G., and De Haan, J. F., "Retrieval of chlorophyll and suspended matter in inland waters from CASI data by matrix inversion," Can. J. Remote Sens., vol. 24, pp. 144-152, 1998.

[16] Lee, Z., Kendall, L. C., Chen, R. F., and Peacock, T. G., “Properties of the water column and bottom derived from Airborne Visible Imaging Spectrometer (AVIRIS) data,” J. Geophys. Res., vol. 106, pp. 11 639-11 652, 2001.

[17] Lee, Z., Carder, K. L., Mobley, C. D., Steward, R. G. and Patch, J. S., “Hyperspectral remote sensing for shallow waters: 2. Deriving bottom depths and water properties by optimization,” Appl. Opt., vol. 38, pp. 3831-3843, 1999.

[18] Brando, V. E., and Dekker, A. G., “Satellite hyperspectral remote sensing for estimating estuarine and coastal water quality,” IEEE Trans. on Geosc. and Rem. Sens., vol. 41(6), pp. 1378-1387, 2003.

[19] Sathyendranath, S., Prieur, L. and Morel, A., “A three-component model of ocean colour and its application to remote sensing of phytoplankton pigments in coastal waters,” Int. J. Remote Sensing, vol. 10, pp. 1373-1394, 1989.

[20] Neumann, A., Hetscher, M., Krawczyk, H., and Tschentscher, C., “Methodological aspects of principal component inversion for case II applications,” in Proc. 2nd International Workshop on MOS-IRS and Ocean Color, Berlin, Germany, pp. 163-170, 1998.

[21] Fischer, J., “On the information content of multispectral radiance measurements over an ocean,” Int. J. Remote Sensing, vol. 6, pp.773-786, 1985.

[22] Sathyendranath, S., Hoge, F. E., Platt, T. and Swift, R. N., “Detection of phytoplankton pigments from ocean colour: Improved algorithms,” Appl. Optics, vol. 33, pp. 1081-1089, 1994.

[23] Lee, Z. P., Zhang, M. R., Carder, K. L. and Hall, L. O., “A neural network approach to deriving optical properties and depths of shallow waters,” in Proc. Ocean Optics XIV, Office of Naval Research, Washington, DC., 1998.

[24] Cipollini, P., Corsini, G., Diani, M., and Grasso, R., “Retrieval of sea water optically active parameters from hyperspectral data by means of generalized radial basis function neural networks,” IEEE Trans. on Geosc. and Rem. Sens., vol. 39(7), pp. 1508-1524, 2001.

[25] D’Alimonte, D., Zibordi, G., and Berthon, J.-F., “Determination of CDOM and NPPM absorption coefficient spectra from coastal water remote sensing reflectance,” IEEE Trans. on Geosc. and Rem. Sens., vol. 42(8), pp. 1770-1777, 2004.

[26] Corsini, G., Diani, M., and Grasso, R., “Radial basis function and multilayer perceptron neural networks for sea water optically active parameter estimation in case II waters: a comparison,” Int. J. Rem. Sens., vol. 24(20), pp. 3917-3932, 2003.

[27] Sandidge J. C., and Holyer, R. J., “Coastal bathymetry from hyperspectral observations of water radiance," Rem. Sens. Environ., vol. 65, pp. 341-352, 1998.

[28] Zadeh, L. A., “Fuzzy sets,” Information and Control, vol. 8(3), pp. 338-353, 1965.

[29] Cococcioni, M., Lazzerini, B., and Marcelloni, F., “Estimating the concentration of optically active constituents of sea water by Takagi-Sugeno models with quadratic rule consequents,” Pattern Recognition vol. 40, pp. 2846-2860, 2007.

[30] Cococcioni, M., Corsini, G., Lazzerini, B., and Marcelloni, F., “Solving the ocean color inverse problem by using multi-objective optimization of neuro-fuzzy

systems," Int. J. of Knowledge-based and Intelligent Engineering Systems (KES), IOS press, vol. 12(5-6), pp. 339-355, 2008.

[31] Fonlupt, C., "Solving the ocean color problem using a genetic programming approach," Appl. Soft Comput., vol. 1, pp. 63-72, 2001.

[32] Zhan, H., Lee, Z., Shi, P., Chen, C., and Carder, K. L., "Retrieval of water optical properties for optically deep waters using genetic algorithms," IEEE Trans. on Geosc. and Rem. Sens., vol. 41(5), pp. 1123-1128, 2003.

[33] Haykin, S., "Neural Networks: A comprehensive foundation," Englewood Cliffs, NJ, Prentice-Hall,. 1994.

[34] Jang, J.-S. R., "ANFIS: adaptive-network-based fuzzy inference systems," IEEE Trans. Syst. Man. Cybernet., vol. 23(3), pp. 665-685, 1993.

[35] Takagi, T., and Sugeno, M., "Fuzzy identification of systems and its application to modeling and control," IEEE Trans. Syst. Man Cybernet., vol. 15, pp. 116-132, 1985.

[36] Lin, C.-T., and Lee, C. S. G., "Neural-network based fuzzy logic control and decision system," IEEE Trans. Computers, vol. 40(12), pp. 1320-1336, 1991.

[37] Vapnik, V., "Estimation of dependences based on empirical data," Springer-Verlag, New York, 1982.

[38] Burges, C. J. C., "A tutorial on Support Vector Machines for pattern recognition," Data Mining and Knowledge Discovery, vol. 2, pp. 121-167, 1998.

[39] Cortes C., and Vapnik, V., "Support vector networks," Mach. Learn., vol. 20, pp. 273-297, 1995.

[40] Cauwenberghs, G., and Poggio, T., "Incremental and decremental support vector machine learning," Adv. Neural Information Processing Systems (NIPS*2000), Cambridge, MA: MIT Press, vol. 13, 2001.

[41] Oceana, "The dumping of hydrocarbons from ships into the seas and oceans of Europe - The other side of oil slicks", 26 pp., 2003.

[42] Kluser, S., Richard, J. P, Giuliani, G., De Bono, A., and Peduzzi, P., "Illegal oil discharge in European seas," Coll. Environment Alert Bulletin, UNEP/DEWA-Europe/GRID-Geneva, 4 pp., 2006.

[43] Killops, S. D., and Killops, V. J., "An introduction to organic geochemistry," Longman, 1993.

[44] North, F. K, "Petroleum geology," Allen & Unwin, 1985.

[45] Ryder, A. G., "Analysis of crude petroleum oils using fluorescence spectroscopy," Reviews in Fluorescence, Annual volumes 2005, pp. 169-198, 2005.

[46] Osadchy, V., U., Shifrin, K. S., and Gurevich, I. Y., "Remote sensing and measurement of the thickness of oil films on the sea surface using the reflectivity contrast," Ocean Optics XII, SPIE Vol. 2258, pp. 747-758, 1994.

[47] Byfield, V., and Boxall, S. R., "Thickness estimates and classification of surface oil using passive sensing at visible and near-infrared wavelengths," in Proc. of IEEE IGARSS'99, vol. 3, pp. 1475-1477, 1999.

[48] Byfield, V., "Optical remote sensing of oil in the marine environment," Ph.D. Thesis, University of Southampton, 1998.

[49] Otremba, Z., and Piskozub, J., "Modelling of the optical contrast of an oil film on a sea surface," Optics Express, vol. 9(8), pp. 411-416, 2001.

[50] Otremba, Z., and Piskozub, J., “Modeling the remotely sensed optical contrast caused by oil suspended in the sea water column,” Optics Express, vol. 11(1), pp. 2-6, 2003.

[51] Brekke, C., and Solberg, A. H. S., “Oil spill detection by satellite remote sensing,” Rem. Sens. Env., vol. 95, pp. 1-13, 2005.

[52] Fingas, M. F., and Brown, C. E., “Review of oil spill remote sensing,” Spill Science and Technology Bulletin, vol. 4, pp. 199-208, 1997.

[53] Alpers, W., and Huhnerfuss, H., “The damping of ocean waves by surface films: A new look at an old problem,” J. Geophys. Res, vol. 94(C5), 6251-6265, 1989.

[54] Liu, A. K., Wu, S. Y., Tseng, W. Y., and Pichel, W. G., “Wavelet analysis of SAR images for coastal monitoring,” Can. J. Rem. Sens., vol. 26, pp. 494-500, 2000.

[55] Robinson, I. S., “Satellite oceanography. An introduction for oceanographers and remote-sensing scientists,” Wiley–Praxis series in remote sensing, 1994.

[56] Kubat, M., Holte, R. C., and Matwin, S., “Machine learning for the detection of oil spills in Satellite radar images,” Mach. Learn., vol. 30, pp. 195-215, 1998.

[57] Del Frate, F., Petrocchi, A., Lichtenegger, J., and Calabresi, G., “Neural networks for oil spill detection using ERS-SAR data,” IEEE Trans. on Geosc. and Rem. Sens., vol. 38, pp. 2282-2287, 2000.

[58] Topouzelis, K., Karathanassi, V., Pavlakis, P., and Rokos, D., “Oil spill detection using RBF Neural Networks and SAR data,” in Proc. of XXth ISPRS Congress. Istanbul, Turkey, 2004.

[59] Solberg, A. H., Storvik, G., Solberg, R., and Volden, E., “Automatic detection of oil spills in ERS SAR images,” IEEE Trans. on Geosc. and Rem. Sens., vol. 37, pp. 1916-1924, 1999.

[60] Solberg, A. H., and Solberg, R., “A large-scale evaluation of features for automatic detection of oil spills in ERS SAR images,” in Proc. of IEEE IGARSS’96, pp. 1484-1486, 1996.

[61] Fiscella, B., Giancaspro, A., Nirchio, F., Pavese, P., and Trivero, P., “Oil spill detection using marine SAR images,” International Journal of Remote Sensing, vol. 21, pp. 3561-3566, 2000.

[62] Keramitsoglou, I., Cartalis, C., and Kiranoudis, C. T., “Automatic identification of oil spills on satellite images,” Environmental Modelling and Software, vol. 21, pp. 640-652, 2006.

[63] Hu, C., Müller-Krager, F. E., Taylor, C. J., Myhre, D., Murch, B., Odriozola, A. L., et al., “MODIS detects oil spills in Lake Maracaibo, Venezuela,” EOS, Trans., American Geophysical Union, vol. 84(33), pp. 313-319, 2003.

[64] Alawadi, F., Amos, C., Byfield, V., and Petrov, P., “The application of hyperspectral image techniques on MODIS data for the detection of oil spills in the RSA,” Proc. of SPIE Vol. 7110, pp. 71100Q-71100Q-12, 2008.

[65] Hu, C., Li, X., Pichel, W. G., and Muller-Karger, F. E., “Detection of natural oil slicks in the NW Gulf of Mexico using MODIS imagery,” Geophys. Res. Lett., vol. 36, L01604, 2009.

[66] NASA’s MODIS level 1 data products, available at: http://ladsweb.nascom.nasa.gov/data/.

[67] Cococcioni, M., Corucci, L., and Lazzerini, B., “Issues and preliminary results in oil spill detection using optical remotely sensed images,” in Proc. of OCEANS’09-IEEE, Bremen, Germany, 2009.

[68] Provost, F., and Fawcett, T., “Robust classification for imprecise environments,” Mach. Learn., vol. 42, pp. 203-231, 2001.

[69] The MathWorks Inc., “Fuzzy Logic Toolbox 2 User’s Guide”, 2009.

[70] Jang, J.-S. R., “Fuzzy modeling using generalized neural networks and Kalman filter algorithm,” Proc. 9th National Conf. Artificial Intel. (AAAI-91), pp. 762-767, 1991.

[71] Corucci, L., Nardelli, F., and Cococcioni, M., “Building a time variant cost-oriented classifier using an ensemble of SVMs on a real case application,” in Proc. of IEEE SMC 2010 Conference, Istanbul, Turkey, 2010.

[72] Flach, P. A., and Wu, S., “Repairing concavities in ROC curves,” in Proc. 2003 UK Workshop on Computational Intelligence, pp. 38-44, 2003.

[73] Polcyn, F. C., and Sattinger, I. J., “Water depth determination using remote sensing techniques," in Proc. of the 6th Int. Symp. Remo. Sens. Environ., pp.1017-1028, Ann Arbor, MI, 1969.

[74] Lyzenga, D. R., “Passive remote sensing techniques for mapping water depth and bottom features,” Appl. Opt., vol. 17(3), pp. 379-383, 1978.

[75] Polcyn, F. C., Brown, W. L., and Sattinger, I. J., “The measurement of water depth by remote-sensing techniques,” Report 8973-26-F, Willow Run Laboratories, Univ. Michigan, Ann Arbor, MI, 1970.

[76] Benny, A. H., and Dawson, G. J., “Satellite imagery as an aid to bathymetric charting in the Red Sea,” Cartographic J., vol. 20(1), pp. 5-16, 1983.

[77] Paredes, J. M., and Spero, R. E., “Water depth mapping from passive remote-sensing data under a generalized ratio assumption,” Appl. Opt., vol. 22, pp. 1134-1135, 1983.

[78] Maritorena, S., Morel, A., and Gentili, B., “Diffuse reflectance of oceanic shallow waters: Influence of water depth and bottom albedo,” Limnol. Oceanog., vol. 39(7), pp. 1689-1703, 1994.

[79] Adler-Golden, S. M., Acharya, P. K., Berk, A., Matthew, M. W., and Gorodetzky, D., “Remote bathymetry of the littoral zone from AVIRIS, LASH, and QuickBird imagery,” IEEE Trans. on Geosc. and Rem. Sens., vol. 43(2), pp. 337-347, 2005.

[80] Grasso, R., Trees, C., Spina, F., and Legac, J. C., “Bathymetry estimation in littoral areas by fusing multispectral satellite data and depth samples from AUVs,” Poster contribution at the 2007 Rapid Environmental Assessment Conference (REA’07), Lerici, Italy, 2007.

[81] Inoue, A. and Kilian, L., “In-sample or out-of-sample tests of predictability: which one should we use?” ECB Working Paper No. 195, 2002. Available at: http://ssrn.com/abstract=358500